Earth System Model Aerosol-Cloud Diagnostics Package (ESMAC Diags) Version 2: Assessments of Aerosols, Clouds and Aerosol-Cloud Interactions Through Field Campaign and Long-Term Observations

Shuaiqi Tang[1], Adam C. Varble[1], Jerome D. Fast[1], Kai Zhang[1], Peng Wu[1], Xiquan Dong[2], Fan Mei[1], Mikhail Pekour[1], Joseph C. Hardin[3], and Po-Lun Ma[1]

[1]Pacific Northwest National Laboratory, Richland, WA, USA
[2]University of Arizona, Tucson, AZ, USA
[3]Unaffiliated scientist

Correspondence to: Shuaiqi Tang (shuaiqi.tang@pnnl.gov)

Abstract.

Poor representations of aerosols, clouds and aerosol-cloud interactions (ACI) in Earth System Models (ESMs) have long been the largest uncertainties in predicting global climate change. Huge efforts have been made to improve the representation of these processes in ESMs, and key to these efforts is evaluation of ESM simulations with observations. Most well-established ESM diagnostics packages focus on the climatological features; however, they are lacking process-level understanding and representations of aerosols, clouds, and ACI. In this study, we developed an ESM aerosol-cloud diagnostics package (ESMAC Diags) to facilitate routine evaluation of aerosols, clouds and aerosol-cloud interactions simulated by the Department of Energy's (DOE) Energy Exascale Earth System Model (E3SM). This paper documents its version 2 functionality (ESMAC Diags v2), which has substantial updates from its version 1 (Tang et al., 2022a). The simulated aerosol and cloud properties have been extensively compared with in-situ and remote-sensing measurements from aircraft, ship, surface and satellite platforms in ESMAC Diags v2. It currently includes six field campaigns and two permanent sites covering four geographical regions: Eastern North Atlantic, Central U.S., Northeastern Pacific and Southern Ocean, where frequent liquid or mixed-phase clouds are present and extensive measurements are available from the DOE Atmospheric Radiation Measurement user facility and other agencies. ESMAC Diags v2 generates various types of single-variable and multi-variable diagnostics, including percentiles, histograms, joint histograms and heatmaps, to evaluate model representation of aerosols, clouds, and ACI. Select examples highlighting ESMAC Diags capabilities are shown using E3SM version 2 (E3SMv2). E3SMv2 in general can reasonably reproduces many observed aerosol and cloud properties, with biases in some variables such as aerosol particle and cloud droplet sizes and number concentrations. The coupling of aerosol and cloud number concentrations may be too strong in E3SMv2, possibly indicating a bias in processes that control aerosol activation. Furthermore, the liquid water path response to perturbed cloud droplet number concentration behaves differently in E3SMv2 and observations, which warrants a further study to improve the cloud microphysics parameterizations in E3SMv2.

1. Introduction

38

39 Poor representations of aerosols, clouds and aerosol-cloud interactions (ACI) in Earth System Models
40 (ESMs) have long been the largest uncertainties in predicting global climate change (Ipcc, 2021).
41 Challenges come from several aspects: first, there are many aerosol properties (e.g., number, size, phase,
42 shape, composition) and cloud micro- and macro-physical properties (e.g., fraction, water content,
43 number and size of liquid and ice hydrometeors) that affect Earth's climate. Coincident measurements of
44 these properties remain largely under-sampled due to substantial spatiotemporal variability and logistical
45 difficulties for making such measurements. Second, there are complex interactive processes between
46 aerosols, clouds, and ambient meteorological conditions, many of which are not fully understood, but are
47 critical to properly interpreting relationships between observable properties. Third, many ACI processes
48 are nonlinear, multi-scale processes that involve feedbacks depending on cloud types and meteorological
49 regimes, which also shift in space and time, presenting challenges for assessing causal effect and
50 representing such processes in ESMs.

51 Huge efforts have been made to improve the representation of aerosols, clouds and ACI in ESMs. Key to
52 these efforts is evaluation of ESM simulations with observations. Many modeling centers have developed
53 standardized diagnostics packages to document ESM performance. For aerosol and cloud properties, most
54 diagnostic packages rely heavily on satellite measurements as evaluation data (e.g., Amwg, 2021; E3sm,
55 2021; Eyring et al., 2016; Gleckler et al., 2016; Maloney et al., 2019; Myhre et al., 2013; Schulz et al.,
56 2006). Satellite remote sensing measurements have global or near global coverage but limited spatial and
57 temporal resolution. They are also facing many challenges to retrieve some variables, especially for
58 aerosol properties such as number concentration, size distribution, chemical composition etc. Some recent
59 studies (e.g., Choudhury and Tesche, 2022) have retrieved cloud condensation nuclei (CCN) number
60 concentration from satellite measurements, which provides a great addition to investigate ACI in global
61 scale. However, large uncertainties exist in satellite retrievals, even for more sophisticated retrieved cloud
62 microphysical properties such as droplet number concentration (e.g., Grosvenor et al., 2018). This limits
63 their application to robustly quantify aerosols, clouds and ACI processes. In-situ measurements from
64 ground, aircraft or ship platforms from field campaigns are also used in a few projects to evaluate ESMs
65 (e.g., Reddington et al., 2017; Watson-Parris et al., 2019; Tang et al., 2022a; Zhang et al., 2020). Some of
66 these field campaigns were conducted over remote or poorly sampled locations, which are highly valuable
67 for model evaluation despite limited spatial coverage and time periods. Moreover, the U.S. Department of
68 Energy (DOE) Atmospheric Radiation Measurement (ARM) user facility has conducted continuous field
69 measurements at a few sites for multiple years. These long-term high-resolution field measurements have
70 also been demonstrated to be valuable for evaluating ESMs (e.g., Zhang et al., 2020).

71 In response to the need for more ESM diagnostics for evaluating ACI processes, Tang et al. (2022a)
72 developed an ESM aerosol-cloud diagnostics package (ESMAC Diags) to facilitate the routine evaluation
73 of aerosols, clouds and ACI simulated by the Department of Energy's (DOE) Energy Exascale Earth
74 System Model (E3SM, Golaz et al., 2019). It includes diagnostics that leverage in-situ measurements
75 from multiple platforms during six field campaigns since 2013, which are not included in previous
76 diagnostics tools (e.g., Reddington et al., 2017). Version 1 of ESMAC Diags (ESMAC Diags v1, Tang et
77 al., 2022a) mainly focuses on aerosol properties. We present here version 2 of ESMAC Diags (ESMAC
78 Diags v2) that is a direct extension of ESMAC Diags v1 with two major additions:

79   1. measurements from satellite and long-term diagnostics at the ARM Southern Great Plains
80 (SGP) and Eastern North Atlantic (ENA) sites.

81   2. diagnostics for cloud properties and aerosol-cloud interactions.

82 The new measurements, as well as major data quality controls are introduced in Section 2. Additional
83 discussions on retrieval uncertainties of cloud microphysical properties are performed in Section 3.
84 Details of the code structure of ESMAC Diags v2, which is substantially changed since version 1, are
85 described in Section 4. Section 5 provides selected examples of single-variable and multi-variable
86 diagnostics using ESMAC Diags v2 to highlight its capabilities. Lastly, Section 6 provides a summary.

2. Aerosol and cloud measurements from ground, aircraft, ship and satellite platforms

88 Following the initial development in version 1, ESMAC Diags v2 continues to focus on six field
89 campaigns conducted in four geographical regions: the Central U.S. (CUS, where the ARM Southern
90 Great Plains (SGP) site is located), Eastern North Atlantic (ENA), Northeastern Pacific (NEP), and
91 Southern Ocean (SO). Information on the six field campaigns is shown in Table 1 and their locations are
92 shown in Figure 1, each reproduced from Table 1 and Figure 3 in Tang et al. (2022a).

93
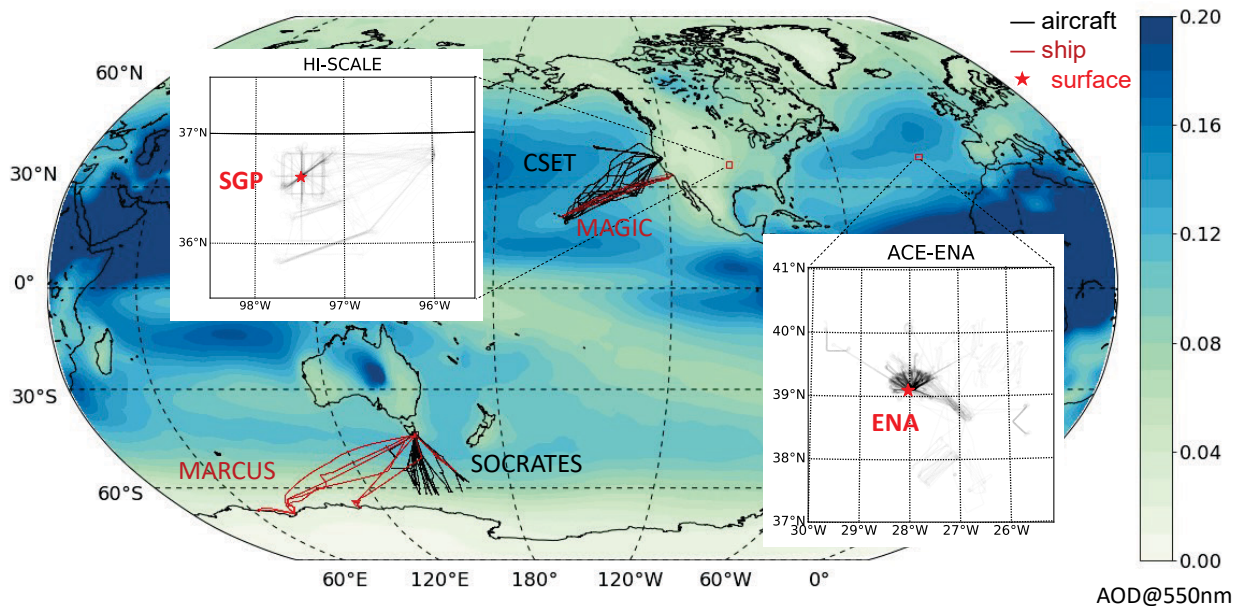
94

95 Figure 1. Aircraft (black) and ship (red) tracks for the six field campaigns. Red stars in
96 the enlarged map indicate two ARM fixed sites: SGP and ENA, that have long-term
97 measurements available for model diagnostics. Overlaid is aerosol optical depth at 550nm
98 averaged from 2014 to 2018 simulated in E3SMv1. (Reproduced from Figure 3 in Tang et
99 al., 2022a)

100 Table 1. Descriptions of the field campaigns used in this study. (Reproduced from Table 1
101 in Tang et al., 2022a)

Campaign*	Period	Platform	Typical Conditions	Reference

HI-SCALE	IOP1: 24 Apr – 21 May 2016 IOP2: 28 Aug – 24 Sep 2016	Ground, aircraft (IOP1: 17 flights, IOP2: 21 flights)	Continental cumulus with high aerosol loading	(Fast et al., 2019)
ACE-ENA	IOP1: 21 Jun – 20 Jul 2017 IOP2: 15 Jan – 18 Feb 2018	Ground, aircraft (IOP1: 20 flights, IOP2: 19 flights)	Marine stratocumulus with low aerosol loading	(Wang et al., 2021)
MAGIC	Oct 2012 – Sep 2013	Ship (18 legs)	Marine stratocumulus to cumulus transition with low aerosol loading	(Lewis and Teixeira, 2015; Zhou et al., 2015)
CSET	1 Jul – 15 Aug 2015	Aircraft (16 flights)	Same as above	(Albrecht et al., 2019)
MARCUS	Oct 2017 – Apr 2018	Ship (4 legs)	Marine liquid and mixed phase clouds with low aerosol loading	(Mcfarquhar et al., 2021)
SOCRATES	15 Jan – 24 Feb, 2018	Aircraft (14 flights)	Same as above	(Mcfarquhar et al., 2021)

102 * Full names of the listed field campaigns:
103 HI-SCALE: Holistic Interactions of Shallow Clouds, Aerosols and Land Ecosystems
104 ACE-ENA: Aerosol and Cloud Experiments in the Eastern North Atlantic
105 MAGIC: Marine ARM GCSS Pacific Cross-section Intercomparison (GPCI) Investigation of Clouds
106 CSET: Cloud System Evolution in the Trades
107 MARCUS: Measurements of Aerosols, Radiation and Clouds over the Southern Ocean
108 SOCRATES: Southern Ocean Cloud Radiation and Aerosol Transport Experimental Study
109

110 The collection and processing of observations are the most time-consuming part of developing ESMAC
111 Diags, which also impacts the reliability of conclusions drawn from the model diagnostics. In this section,
112 we introduce the data used in ESMAC Diags v2, existing quality issues in some datasets, and treatments
113 to address these quality issues. Some variables are difficult to directly measure or have limited in-situ
114 sampling and thus must be derived from remote sensing measurements using retrieval algorithms. In
115 Section 3, we further discuss the uncertainty and reliability of some cloud retrieval products via
116 comparisons with in-situ aircraft measurements.

117 2.1. Data availability

118 All measurements, instruments, and data products used in the six field campaigns and two long-term sites
119 in ESMAC Diags v2 are shown in Table 2. Further details of the measurements, data product names, and
120 DOIs are given in Tables S1 to S6 (for field campaigns) and Tables S7 and S8 (for SGP and ENA sites) in
121 the supplementary material. To allow maximum overlapping of key measurements while also ensuring a
122 long enough period for statistical evaluation, we select the periods of 1 Jan 2011 – 31 Dec 2020 for SGP
123 and 1 Jan 2016 – 31 Dec 2018 for ENA for long-term analyses. In addition to the aerosol measurements
124 discussed in Tang et al. (2022a), we incorporate more cloud and radiation measurements, as well as
125 geostationary satellite retrievals using Visible Infrared Solar-Infrared Split Window Technique (VISST)
126 (Minnis et al., 2008; Minnis et al., 2011) algorithm. The VISST products archived by ARM cover
127 approximately 10° by 10° regions in 0.5° by 0.5° resolution centered over ARM sites. Moreover, ARM
128 recently released products consisting of merged aerosol particle and cloud droplet size distributions from

129   aircraft measurements for HI-SCALE and ACE-ENA campaigns. These data are now used in ESMAC
130   Diags v2.

131   Table 2: List of instruments and measurements used in ESMAC Diags v2.

Platform	Measurements	Instruments / data products	Available campaigns
Ground	Surface temperature, relative humidity, wind, pressure, precipitation; upper-level temperature, relative humidity, wind	Surface meteorological station (MET), ARM best estimate (ARMBE) products	HI-SCALE, ACE-ENA, SGP, ENA
	Longwave and shortwave radiation, cloud fraction	ARM best estimate (ARMBE) products	HI-SCALE, ACE-ENA, SGP, ENA
	Aerosol number concentration	Condensation particle counter (CPC), Condensation particle counter – fine (CPCF), Condensation particle counter – ultrafine (CPCU), Ultra-high sensitivity aerosol spectrometer (UHSAS), Scanning mobility particle sizer (SMPS)	HI-SCALE, ACE-ENA, SGP, ENA
	Aerosol size distribution	Ultra-high sensitivity aerosol spectrometer (UHSAS), Scanning mobility particle sizer (SMPS), Nano scanning mobility particle sizer (nanoSMPS)	HI-SCALE, ACE-ENA, SGP, ENA
	Aerosol composition	Aerosol chemical speciation monitor (ACSM)	HI-SCALE, ACE-ENA, SGP, ENA
	CCN number concentration	Cloud condensation nuclei (CCN) counter	HI-SCALE, ACE-ENA, SGP, ENA
	Cloud optical depth	Multifilter rotating shadowband radiometer (MFRSR)	HI-SCALE, ACE-ENA, SGP, ENA
	Cloud droplet number concentration	Cloud droplet number concentration retrieval (Ndrop), cloud retrieval from Wu et al. (2020)	HI-SCALE, ACE-ENA, SGP, ENA
	Cloud droplet effective radius	Multifilter rotating shadowband radiometer (MFRSR), cloud retrieval from Wu et al. (2020)	HI-SCALE, ACE-ENA, SGP, ENA
	Cloud liquid water path	Microwave radiometer (MWR), ARM best estimate (ARMBE) products	HI-SCALE, ACE-ENA, SGP, ENA
	Cloud base height, cloud top height	Active remote sensing of clouds (ARSCL)	HI-SCALE, ACE-ENA, SGP, ENA
Satellite	TOA shortwave and longwave radiation	Geostationary satellite-based retrievals using Visible Infrared Solar-Infrared Split Window Technique (VISST) algorithm	HI-SCALE, ACE-ENA, MAGIC, MARCUS, SGP, ENA
	cloud fraction; height, pressure and temperature at cloud top	Geostationary satellite-based retrievals using Visible Infrared Solar-Infrared Split Window Technique (VISST) algorithm	HI-SCALE, ACE-ENA, MAGIC, MARCUS, SGP, ENA
	liquid water path; cloud optical depth; droplet effective radius	Geostationary satellite-based retrievals using Visible Infrared Solar-Infrared Split Window Technique (VISST) algorithm	HI-SCALE, ACE-ENA, MAGIC, MARCUS, SGP, ENA
	Cloud droplet number concentration	Retrieved from VISST data using the algorithm in Bennartz (2007)	HI-SCALE, ACE-ENA, MAGIC, MARCUS, SGP, ENA
Aircraft	Navigation information and meteorological parameters	Interagency working group for airborne data and telemetry systems (IWG)	HI-SCALE, ACE-ENA
	Aerosol number concentration	Condensation particle counter (CPC), Condensation particle counter – ultrafine (CPCU), Condensation nuclei counter (CNC), Ultra-high sensitivity aerosol spectrometer (UHSAS), Passive cavity aerosol spectrometer (PCASP)	HI-SCALE, ACE-ENA, CSET, SOCRATES

	Aerosol size distribution	Ultra-high sensitivity aerosol spectrometer (UHSAS), Fast integrated mobility spectrometer (FIMS), Passive cavity aerosol spectrometer (PCASP), Best estimate aerosol size distribution (BEASD)	HI-SCALE, ACE-ENA, CSET, SOCRATES
	Aerosol composition	High-resolution time-of-flight aerosol mass spectrometer (AMS)	HI-SCALE, ACE-ENA
	CCN number concentration	Cloud condensation nuclei (CCN) counter	HI-SCALE, ACE-ENA, SOCRATES
	Cloud liquid water content	Water content measuring system (WCM), PMS-King Liquid Water Content (LWC)	HI-SCALE, ACE-ENA, CSET, SOCRATES
	Cloud droplet number size distribution	1DC, 2DC, 2DS, CDP, Cloud probe merged size distribution (mergedSD)	HI-SCALE, ACE-ENA, CSET, SOCRATES
Ship	Navigation information and meteorological parameters	Meteorological station (MET)	MAGIC, MARCUS
	Aerosol number concentration	Condensation particle counter (CPC), Ultra-high sensitivity aerosol spectrometer (UHSAS)	MAGIC, MARCUS
	Aerosol size distribution	Ultra-high sensitivity aerosol spectrometer (UHSAS)	MAGIC, MARCUS
	CCN number concentration	Cloud condensation nuclei (CCN) counter	MAGIC, MARCUS
	Cloud liquid water path	Microwave radiometer (MWR)	MAGIC, MARCUS
	Cloud droplet number concentration, cloud effective radius	Cloud retrieval from Wu et al. (2020)	MAGIC

132

133 All the observational data are quality controlled with their time resolution re-scaled to that suitable for
134 evaluating E3SM, and the rescale resolution can be adjusted to fit for different model output frequencies.
135 Currently, ground, ship and satellite measurements are re-scaled to a 1-hour frequency to be consistent
136 with current E3SM output frequency. Rescaling consists of computing either the median, mean or
137 interpolated value depending on the original data frequency and variable properties. For most aerosol and
138 cloud microphysics measurements, the median value is computed to remove occasional spikes or zeros
139 resulting from data contamination or measurement error. For some bulk cloud properties (e.g., cloud
140 fraction, liquid water path (LWP)), the mean value is computed to be consistent with grid-mean E3SM
141 output. Interpolation is only used when the input frequency is equal to or coarser than the frequency of
142 model output. For aircraft measurements, 1-minute resolution is used to retain high variability and allow
143 matching samples of aerosol and cloud at the same time. To compare with high-frequency aircraft data,
144 E3SM output is interpolated to the same resolution using the nearest grid cell and time slice. Although the
145 current 1-hour, 1-degree E3SM output could not capture the high variability of the aircraft measurements,
146 we are targeting the exascale E3SM version planned in the next few years. In kilometer scale resolution
147 ESM simulations, the high variability in aircraft measurements will be better captured. In the current
148 diagnostics we only focus on the statistics for the entire campaign. As seen later in Section 5.1, coarse-
149 resolution model outputs show similar percentile ranges with the high-resolution aircraft measurements,
150 indicating that for simple percentiles, large-scale variabilities dominate over subgrid variabilities over
151 month-long field campaign periods. Further analysis is needed to understand the importance of other
152 statistics (variance, covariance, etc.) of subgrid scale variabilities. . All processed data are saved in a
153 standardized NetCDF format (Netcdf, 2022) and available for downloading (see data availability section)
154 and direct use.

155 2.2 Data quality issues and treatments

156   Many observation datasets used in ESMAC Diags are ARM level-b (quality-controlled) or level-c (value-
157   added) products, which include quality control (QC) flags to indicate data quality issues. For most
158   datasets, a QC treatment is applied to remove all data with questionable flags. However, there are certain
159   datasets or circumstances in which a QC flag is overly strict (too many good data are removed) or not
160   strict enough (some bad data are not removed). Here we document some of these situations and how we
161   handle them in our data processing.

162   2.2.1 ARM Condensation Particle Counter (CPC) measurements

163   ARM CPC data have several QC values representing failure of different quality checks. One of them
164   checks if the concentration is greater than a maximum allowable value, which is set to 8,000 cm^{-3} for
165   model 3010 (CPC, size detection limit 10 nm), 10,000 cm^{-3} for model 3772 (CPCF, size detection limit 10
166   nm), and 50,000 cm^{-3} for model 3776 (CPCU, size detection limit 3 nm). At SGP, new particle formation
167   (NPF) events occur frequently when CPC and CPCF measurements can exceed 30,000 cm^{-3}. This is much
168   higher than the maximum allowable value but physically reasonable. Simply removing these large values
169   results in an underestimation of aerosol number concentration and produces unrealistic diurnal cycle since
170   they usually occur during the daytime (Tang et al., 2022a). By consulting with the ARM instrument
171   mentor, we only remove data with critical QC flags, but keep data with this QC flag that is overly
172   restrictive.

173   2.2.2 NCAR research flight aerosol number concentration (CN) measurements

174   NCAR research flight (RF) data used in ESMAC Diags do not include QC flags but occasionally show
175   suspiciously large or negative aerosol counts. The following minimum and maximum thresholds are
176   applied to remove suspicious data:

177   • Total CN from a Condensation Nucleation Counter (CNC, reported as CONCN): minimum = 0,
178   maximum = 25,000 cm^{-3}.
179   • Total CN from an Ultra-High-Sensitivity Aerosol Spectrometer (UHSAS, reported as
180   UHSAS100): minimum = 0, maximum = 5,000 cm^{-3}.
181   • Aerosol number size distribution from an UHSAS (reported as CUHSAS_RWOOU or
182   CUHSAS_LWII): minimum = 0, maximum = 500 cm^{-3} per size bin.

183   2.2.3 Ship-measured aerosol properties

184   Aerosol instruments on ships are occasionally contaminated by ship emissions, which present as large
185   spikes in aerosol and CCN number concentrations. For ARM MARCUS measurements, Humphries
186   (2020) published reprocessed CN and CCN data to remove ship exhaust contamination using method
187   described in Humphries et al. (2019). This data is used in this diagnostics package. For MAGIC, we could
188   not find any ship exhaust contamination information. By visually examining the dataset, a simple
189   maximum threshold (25,000 cm^{-3} for CPC, 5,000 cm^{-3} for UHSAS100, 2,000 cm^{-3} for CCN at 0.1%
190   supersaturation and 4,000 cm^{-3} for CCN at 0.5% supersaturation) is applied to remove likely
191   contamination from ship emissions.

192   2.2.4 CCN measurements

There are different supersaturation (SS) setting strategies for CCN measurements. Some aircraft campaigns measured CCN with constant SS (ACE-ENA, HI-SCALE). Some other campaigns measured CCN with time-varying (scanning) SS (SOCRATES, surface CCN counters at SGP and ENA). However, the actual SS in a scanning strategy has fluctuations that are different than the target SS. For the latter, CCN for each SS (0.1%, 0.2%, 0.3% and 0.5%) are obtained by selecting CCN measured within ± 0.05% of the SS target.

For long-term measurements at SGP and ENA, near-hourly CCN spectra data are available, and a quadratic polynomial is fit to the spectra such that CCN number concentration can be estimated at any SS between the measured minimum and maximum SS values. We calculate and output CCN number concentration from these fits at three target supersaturations (0.1%, 0.2% and 0.5%). The fitted spectra data provides CCN number concentration at the exact target supersaturations, but the sample number is slightly smaller due to occasional failure of polynomial fitting.

2.2.5 Contaminated surface aerosol measurements at ENA

The ARM ENA site is located at a local airport. Aerosol measurements at ENA are sometimes contaminated by aircraft and vehicle emissions, rendering the measurements not representative of the background environment. Gallo et al. (2020) identified periods when CPC measurements were likely contaminated from localized emissions (Figure 2a). Their aerosol mask data has 1-min resolution. When we rescale the data to 1-hr resolution and apply the mask on other coarse time-resolution aerosol measurements (e.g., ACSM, Figure 2c), we mask hours in which more than half of the hour is flagged by the aerosol mask. The masking slightly increases the occurrence fraction of small values due to removing many large values, but it does not change the overall distribution (Figure 2b and 2d). A sensitivity analysis was performed, showing that 50% is a reasonable threshold to balance removal of contamination with keeping reasonable data (not shown).
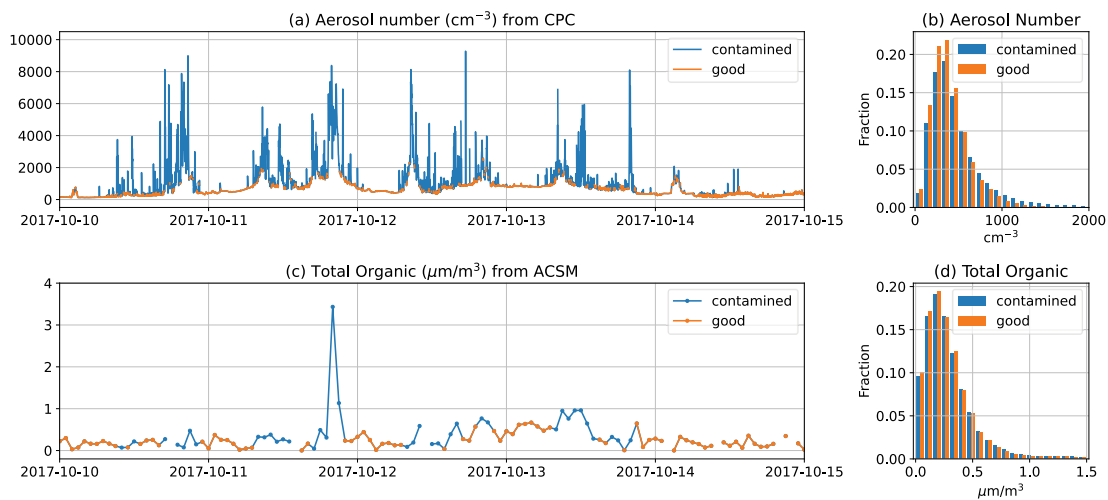
Figure 2: (a) CPC-measured CN from 10 to 15 October 2017 (1-minute resolution) with local contamination flagged by Gallo et al. (2020). (b) histogram of CPC-measured CN for all data from 2016-2018. (c) ACSM measured total organic matter from 10 to 15 October 2017 (1-hour resolution). Hours with more than half or the hour flagged in 1-minute CPC

221   data are masked as contaminated. (d) histogram of ACSM-measured total organic matter
222   for all data from 2016-2018.

223   **3.   Verification of cloud retrievals with in-situ measurements**

224   Cloud microphysical properties such as droplet number concentration (N_d) and effective radius (R_{eff}) are
225   important variables that connect clouds to other aspects in the climate system such as aerosols and
226   radiation. Except in field campaigns where in-situ aircraft measurements are available, remote sensing
227   retrieval algorithms are usually needed to derive these quantities. Several cloud retrieval products from
228   ground and satellite measurements with different algorithms are used in ESMAC Diags v2. This section
229   compares these cloud retrievals with in-situ aircraft measurements to assess retrieval limitation,
230   uncertainty, and utility. N_d and R_{eff} from aircraft measurements taken during HI-SCALE and ACE-ENA
231   field campaigns are calculated from merged cloud droplet number size distributions (mergedSD) from
232   three different cloud probes with different size ranges. The mergedSD covers the size range from 1.5 µm
233   to 9075 µm, covering the entire E3SM cloud droplet size distribution range and extending to rain droplet
234   size range (> 100 µm). For field campaigns used in this study, the aircraft only flied through non-
235   precipitating or drizzling clouds, in which the airborne measurements usually measure rain droplet
236   number 3 to 5 orders of magnitude smaller than cloud droplet number. Therefore, the inclusion of rain
237   droplet size range has ignorable impact on the aircraft-estimated N_d and R_{eff}.

238   Table 3 lists R_{eff} and N_d retrieval products used in ESMAC Diags v2. We retrieved Nd_sat with input
239   data from VISST products using the algorithms described in Bennartz (2007), but assuming a ratio of the
240   drop volume mean radius to R_{eff} (commonly referred to as k) of 0.74 and a cloud adiabaticity of 80%
241   (Varble et al., 2023). Other datasets are all available as released products. All retrievals assume a
242   horizontally homogeneous single-layer liquid phase cloud with constant N_d throughout the cloud layer.
243   However, retrieval algorithms are usually run for all conditions whenever they return valid values. When
244   assumptions are not satisfied, retrieved properties may contain large errors and likely alter statistics such
245   as increasing the occurrence frequency of small N_d as will be shown next.

246   Table 3: Cloud droplet effective radius R_{eff} and number concentration N_d retrievals

Variable	Dataset	Platform	Campaign/site	Retrieved from	Reference
R_{eff}	MFRSRCLDOD	Ground	HI-SCALE, ACE-ENA, SGP, ENA	SW diffuse flux, LWP	(Min and Harrison, 1996; Turner et al., 2021)
	VISST	Satellite	HI-SCALE, ACE-ENA, MAGIC, MARCUS, SGP, ENA	Brightness temperature	(Minnis et al., 2011)
	Wu_etal	Ground	ACE-ENA, MAGIC, ENA	Radar reflectivity, LWP	(Wu et al., 2020)
N_d	Ndrop	Ground	HI-SCALE, ACE-ENA, SGP, ENA	LWP, COD, cloud height	(Riihimaki et al., 2021; Lim et al., 2016)
	Nd_sat (calculated from VISST)	Satellite	HI-SCALE, ACE-ENA, MAGIC, MARCUS, SGP, ENA	LWP, COD, CTT	(Bennartz, 2007)

	Wu_etal	Ground	ACE-ENA, MAGIC, ENA	Radar reflectivity, LWP	(Wu et al., 2020)

247 MFRSRCLDOD: Cloud Optical Properties from the MultiFilter Shadowband Radiometer (MFRSR)

248 SW: shortwave

249 COD: cloud optical depth

250 CTT: cloud top temperature

251

252 Figures 3 shows the occurrence fraction histograms of N_d retrievals with aircraft measurements for HI-

253 SCALE and ACE-ENA field campaigns, with the comparison of original temporal resolution versus 30-

254 minute mean, and the use of all available samples and samples that are filtered as overcast (cloud

255 fraction > 90%) low-level (cloud top height < 4 km) clouds. Figure 4 shows similar plots but for R_{eff}.

256 We also selected two cases with single-layer boundary layer stratus or stratocumulus clouds and plotted

257 their timeseries of original-resolution and 30-min averaged R_{eff} and N_d in Figure S1. The high-frequency

258 aircraft measurements and MFRSR/Ndrop retrievals exhibit much larger variability than coarse-frequency

259 retrievals of Wu_etal and VISST. They frequently sample cloud edges or cloud top/base (for aircraft),

260 where N_d is typically less than further into the cloud. This causes large occurrence fractions in the lowest

261 few bins in the N_d histograms (Figure 3a and 3d). The 30-min VISST products also show large

262 occurrence fraction in the lowest N_d bin for HI-SCALE (Figure 3a), likely due to high frequency of

263 partial cloudy condition over continental U.S. Filtering conditions to only include overcast low-level

264 clouds (Figure 3b, e) and averaging into a coarser resolution (Figure 3c, f) both contribute to the reduction

265 of occurrence fraction in small-N_d bins, and make the measurements from different instruments more

266 comparable.

267
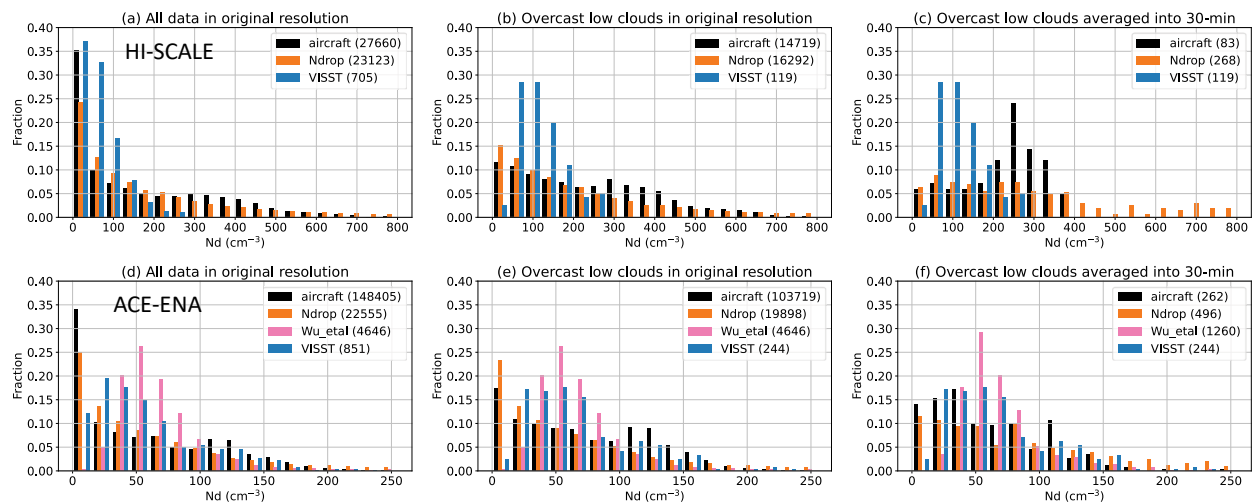
268

269 Figure 3: Histogram of N_d from different measurements/retrievals in (top) HI-SCALE and

270 (bottom) ACE-ENA field campaigns, with total sample numbers in the parentheses. (a) and

271 (d) use data samples in their original resolution (1 s for aircraft measurements, 20 s for

272 Ndrop data, 5 min for Wu_etal data, and 30 min for VISST data). (b) and (e) include only

273 overcast low-cloud situations. For aircraft data, this means N_d is > 1 cm^{-3} for 5 s before

274 and after the sampling time; for Ndrop and VISST data, it means cloud fraction > 90% and

275 cloud top height < 4km. (c) and (f) include only overcast low-cloud situations, and

 average into 30-min resolution. For all the plots, VISST data with solar zenith angle > 65°
are removed to avoid artifact from sunlight.
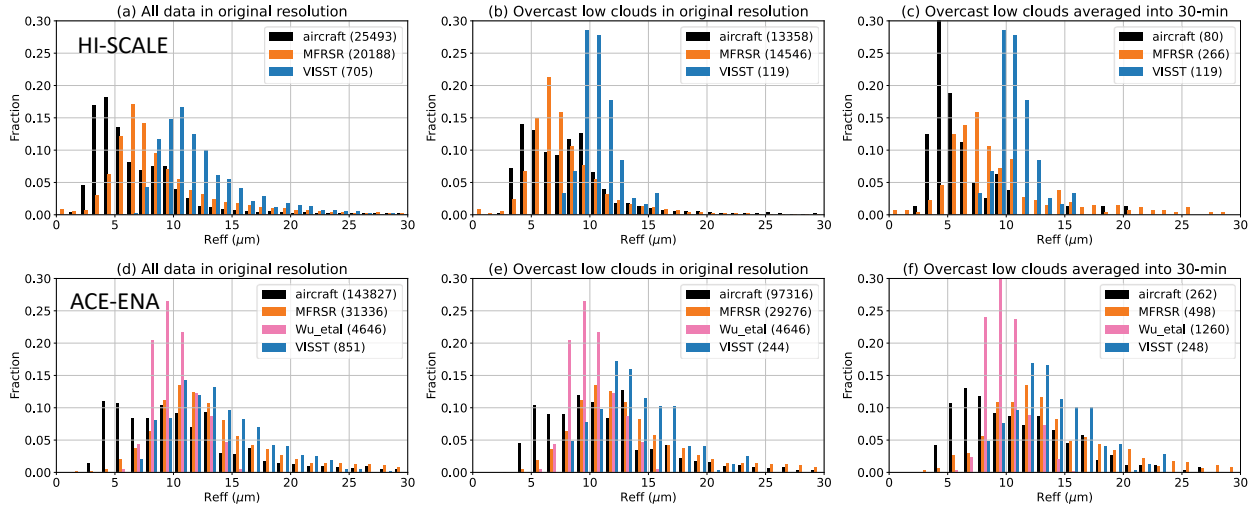
Figure 4: similar as in Figure 3 but for R_{eff}.

Overall, the remote sensing retrievals and aircraft measurements produce reasonable ranges of N_d and R_{eff}. Marine clouds (ACE-ENA) have smaller N_d (Figure 3) and larger R_{eff} (Figure 4) than continental clouds (HI-SCALE). Different retrievals are more consistent with each other for marine clouds than continental clouds. Even after rescaling to the same temporal resolution, aircraft and Ndrop data exhibit broader N_d distributions than satellite retrieval, likely due to their high sampling frequency that may capture more extreme conditions with very high or low N_d. Moreover, the assumption of a fixed adiabaticity (0.8) in satellite retrieval will also narrow N_d distribution. For R_{eff}, we do not expect different datasets to be perfectly agree with each other, as cloud droplet size grows with height in the cloud. All remote sensing retrievals have larger R_{eff} values than aircraft measurements, potentially because remote sensors weight more towards the upper cloud where droplet size and liquid water content (LWC) are larger. Wu_etal retrieves vertical profiles of R_{eff}, and a median value of the R_{eff} profile is used to represent the entire cloud. This makes Wu_etal retrieval weight less toward large droplets thus its R_{eff} is less than MFRSR and VISST. VISST data have the largest R_{eff} values, likely because satellite retrievals reflect conditions at the cloud top. Given the spread in retrieved cloud properties, the limitations and uncertainties of cloud microphysics retrievals clearly need to be considered when they are used to evaluate model performances.

4. Structure of diagnostics package

Figure 5 shows the directory structure of ESMAC Diags v2. It is substantially changed from ESMAC Diags v1 (Tang et al., 2022a). First, we save all data separately as *raw_data,* which stores all input datasets collected from field campaigns, and *prep_data*, which stores preprocessed data with standardized time resolution and quality controls as described in Section 2. The structure is still designed to be flexible for future extension with additional measurements and/or functionality. Second, the diagnostics functions now give users more freedom to modify analyses, such as selecting different time periods, performing

304 additional data filtering or treatments, and examining ACI relationships in specified variable
305 combinations (for scatter plots, joint histograms or heatmaps). We provide a set of example scripts to
306 assist users design their own diagnostics based on their needs. We also provide the source code of data
307 preparation for observations and model output, and a detailed instruction on how to run the code. Users
308 can revise the code to process their own observational data or model output. All the information is
309 available in the ESMAC Diags github repository.
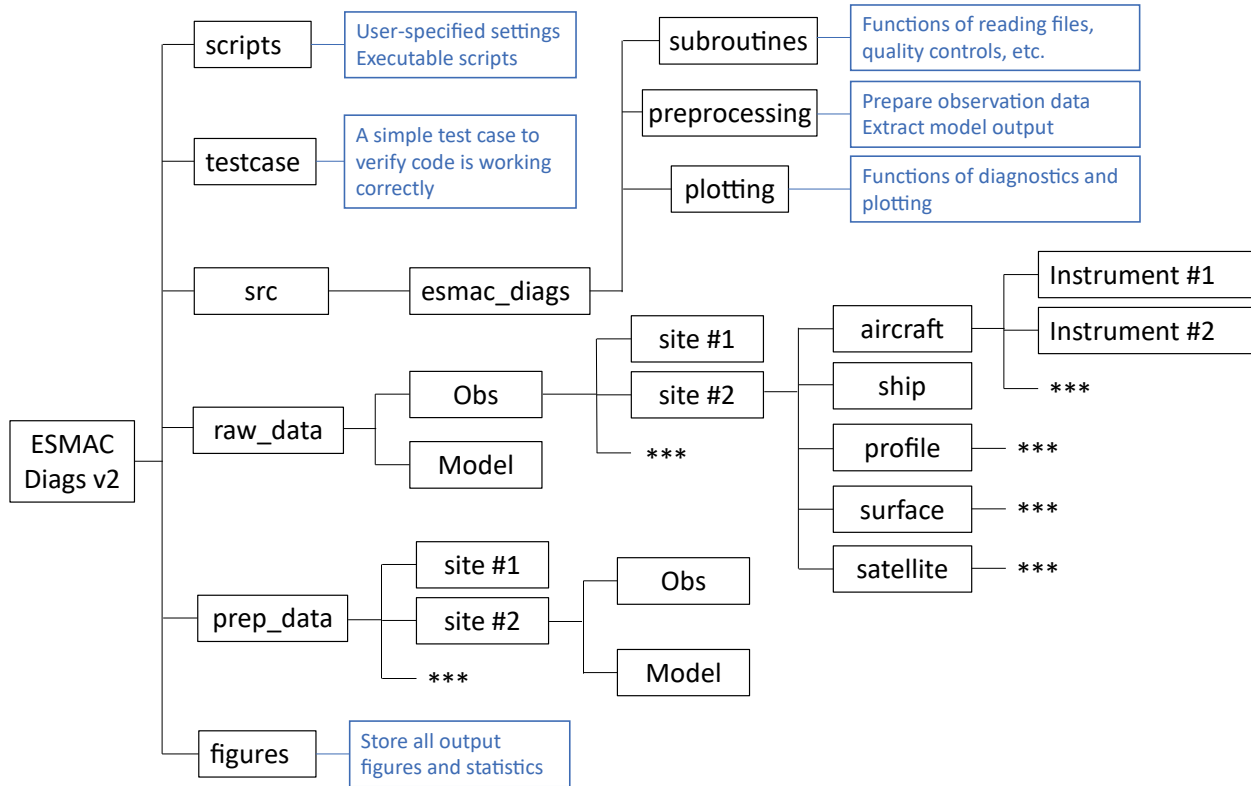
310

311 Figure 5: Directory structure of ESMAC Diags v2. Blue boxes describe the functions of
312 the directory. Asterisks represent boxes that follow the same format as those shown in
313 parallel.

314 ESMAC Diags v1 included diagnostics of aerosol mean statistics (mean, bias, RMSE, correlation),
315 timeseries, diurnal cycle, vertical profiles, mean particle number size distribution, percentiles by
316 height/latitude, and pie/bar charts (Tang et al., 2022a). ESMAC Diags v2 now includes the following new
317 diagnostics that include cloud variables:

318   -   5th, 25th, 50th, 75th and 95th percentiles,
319   -   Seasonal cycle at SGP and ENA,
320   -   Histograms for individual variables,
321   -   Scatter plots,
322   -   Joint histograms of two variables, and
323   -   Heatmaps of three variables (mean of one variable binned by two other variables).

324 The inclusion of two-variable scatter plots, joint histograms, and three-variable heatmaps provides the
325 functionality to study ACI-related relationships. We present a few examples in the next section to
326 demonstrate these new diagnostics.

327
328 **5. Diagnostics Examples**

329 In this section, we show some examples of diagnostics applied to E3SM version 2 (E3SMv2) (Golaz et
330 al., 2022). Compared to the aerosol and cloud parameterizations in E3SMv1 (Rasch et al., 2019; Golaz et
331 al., 2019), E3SMv2 updated the treatments on dust particles, incorporated recalibration of parameters (Ma
332 et al., 2022), changed the call order and refactored the code of the Cloud Layers Unified By Binormals
333 (CLUBB) parameterization, and retuned some parameters (Golaz et al., 2022). We constrain the model
334 simulations by nudging the horizontal winds towards the 3-hourly Modern-Era Retrospective analysis for
335 Research and Applications, Version 2 (MERRA-2, Gelaro et al., 2017) with a nudging time scale of 6
336 hour. Previous studies have shown that with nudging, E3SM can well simulate the large-scale circulations
337 in reanalyses (Sun et al., 2019; Zhang et al., 2022). The model was run for individual field campaigns
338 (Table 1) and from 2010 to 2020 for long-term diagnostics at SGP and ENA sites, with hourly model
339 output saved over the field campaign regions for detail evaluation. As described in Section 2, all
340 diagnostics for ground and ship campaigns are in 1-hour resolution while diagnostics for aircraft
341 campaigns are in 1-minute resolution. For aerosol and cloud variables, model raw output variables (not
342 from instrument simulators) are used in this paper to reveal the intrinsic ACI relationships in E3SM.
343 However, as can be seen later in this section, instrument simulators can be better used in some diagnostics
344 to ensure more consistent comparison. Users may choose whether or not to use simulators in their
345 diagnostics depending on their purpose.

346 **5.1. Single-variable diagnostics**

347 Figures 6 and 7 show mean and percentile values of aerosol and cloud properties measured from field
348 campaigns in the four geographical regions: CUS, ENA, NEP and SO. Figure 6 is for aircraft platforms
349 and Figure 7 is for ground or ship platforms with satellite data included when available. Note that the
350 aircraft and ground/ship campaigns may cover different time periods (Table 1), thus some differences
351 seen between aircraft and ship measurements may be caused by seasonal variation. As cloud
352 microphysical properties are usually retrieved with assumptions (Section 3), for ground/ship/satellite data,
353 we only focus on overcast low-level liquid cloud condition here (cloud fraction > 90%, cloud top height <
354 4 km and ice water path < 0.01 mm). E3SM does not output cloud top height, which is derived using a
355 weighting integration method as described in (Varble et al., 2023).

356 From both aircraft and ground/ship data, HI-SCALE has much larger aerosol and cloud droplet number
357 concentrations with smaller droplet sizes compared to other campaigns, which is expected for a
358 continental environment compared to a marine environment. The cloud optical depth is also greater for
359 HI-SCALE than other campaigns, which is driven by smaller droplet sizes rather than LWP differences.
360 Satellite retrievals generally produce smaller N_d, LWP, and cloud optical depth with greater R_{eff} than
361 surface retrievals. As discussed in Section 3, retrieval uncertainties need to be kept in mind when these
362 retrieved microphysical properties are used to evaluate models.

363   E3SMv2 overestimates CN (> 10 nm) over CUS, ENA and NEP. Larger particle concentration (CN > 100
364   nm) is generally underestimated over CUS and overestimated over ENA and NEP. Over SO, E3SMv2
365   produces fewer small aerosol particles (CN > 10 nm) and about the same number of large aerosol
366   particles (CN > 100 nm) compared to the observations. These results are confirmed by both aircraft and
367   ground/ship campaigns, except for the HI-SCALE aircraft campaign where small particles from local
368   emissions were occasionally observed but unable to be simulated. These results are consistent with our
369   previous diagnostics for E3SMv1 (Tang et al., 2022a). E3SMv2 also underestimates N_d over CUS and
370   SO, which corresponds with the underestimation of accumulation mode (> 100 nm) CN over CUS but
371   underestimation of Aitken mode (> 10 nm) CN over SO. It is possible that over very clean regions such as
372   SO, small particles are more important in cloud formation than over continental regions such as CUS.
373   Simulated LWP (LWC) is generally consistent with satellite (aircraft) measurements, but smaller than
374   ground/ship measurements, which may be partly caused by rain contamination of ground/ship retrievals.
375   R_{eff} evaluation is less certain given large discrepancies between satellite and ground retrievals.
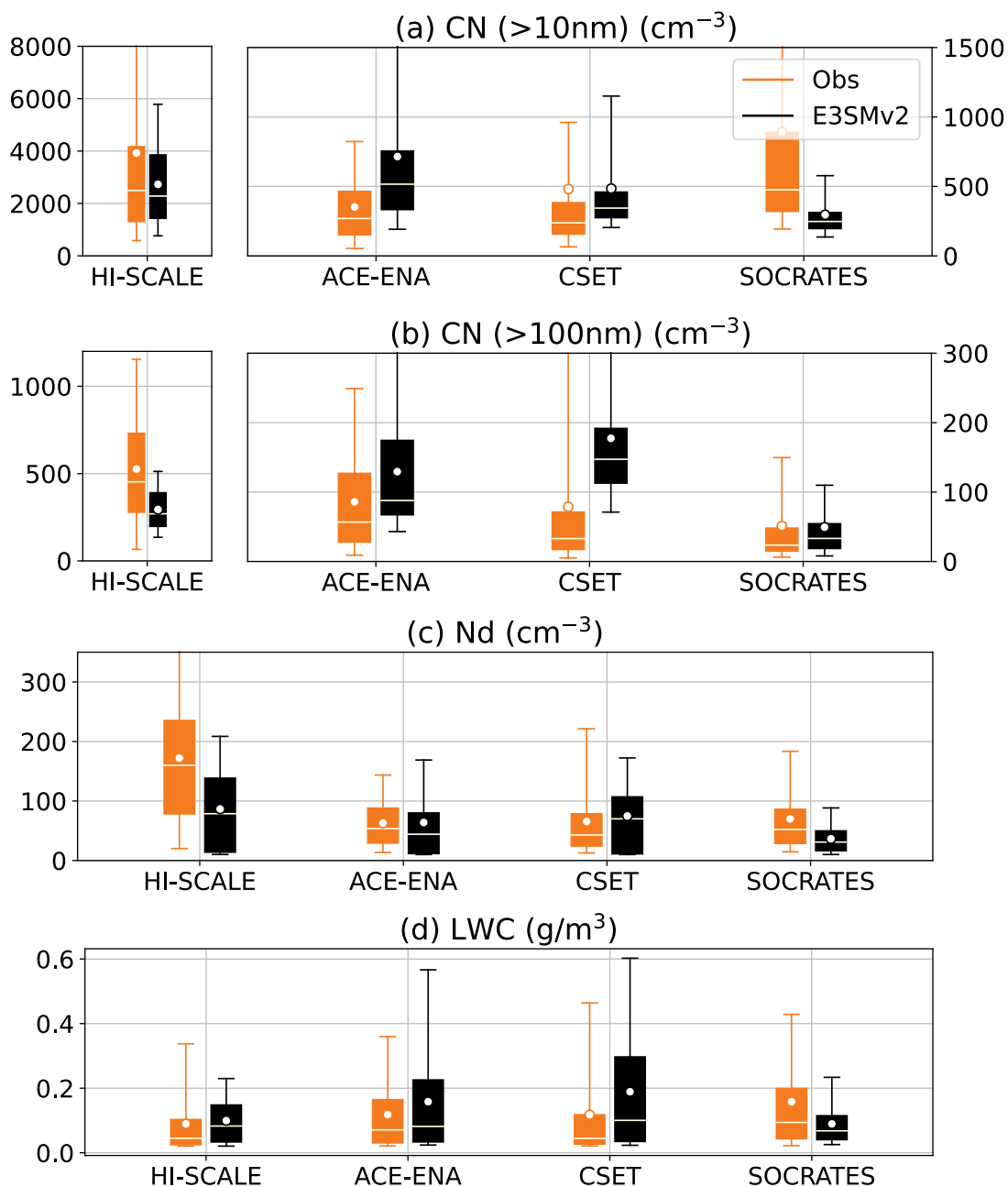
Figure 6: Box-whisker plots of (a) CN for size > 10 nm, (b) CN for size > 100 nm, (c) in-cloud N_d, (d) LWC for all data from aircraft field campaigns at CUS, ENA, NEP and SO regions from left to right. Boxes denote 25th and 75th percentiles, whiskers denote 5th and 95th percentiles, the white horizontal line represents median values, and the white dot represents mean values. For aerosol number concentrations, the y axes for HI-SCALE are separated from other field campaigns for better visualization. The top whiskers that are out of the y-axis range are: (a) HI-SCALE obs: 13681. ACE-ENA E3SMv2: 2061. SOCRATES obs: 2745. (b): ACE-ENA E3SMv2: 304. CSET obs: 305. CSET E3SMv2: 400. (c): HI-SCALE obs: 397.
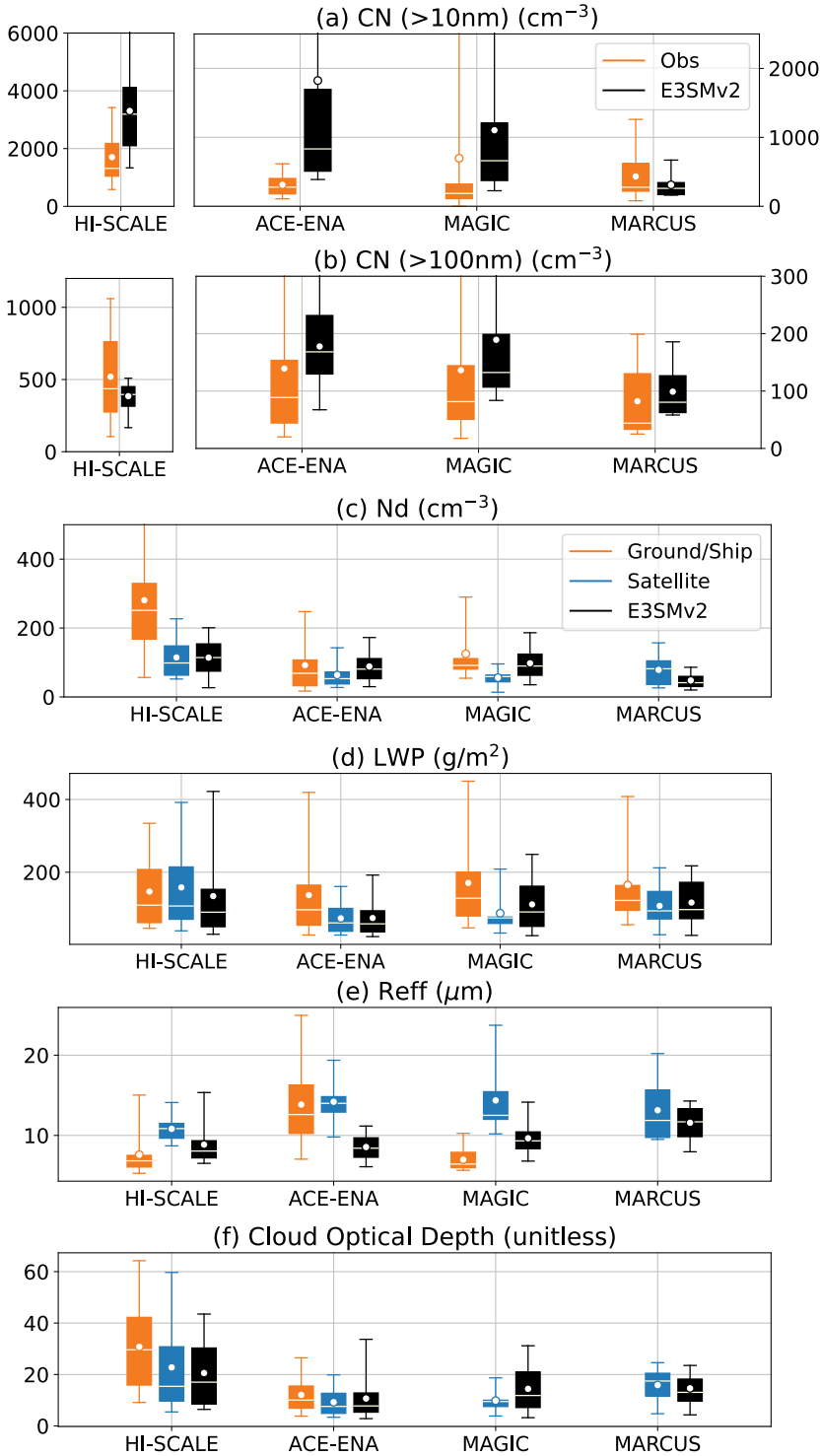
Figure 7: Box-whisker plots of (a) CN for size > 10 nm, (b) CN for size > 100 nm, (c) layer-mean N_d, (d) LWP, (e) R_{eff}, (f) cloud optical depth for overcast low-level liquid cloud conditions (cloud top height < 4 km, cloud fraction > 90% and ice water path < 0.01 mm) in ground and ship field campaigns at CUS, ENA, NEP and SO regions from left to right. Boxes denote 25th and 75th percentiles, whiskers denote 5th and 95th percentiles, the

white horizontal line represents median values, and the white dot represents mean values. For aerosol number concentrations, the y axes for HI-SCALE are separated from other field campaigns for better visualization. The top whiskers that are out of the y-axis range are: (a) HI-SCALE E3SMv2: 6102. ACE-ENA E3SMv2: 7575. MAGIC obs: 3330. MAGIC E3SMv2: 3771. (b): ACE-ENA obs: 304.7. ACE-ENA E3SMv2: 328.3. MAGIC obs: 377.7. MAGIC E3SMv2: 577.8. (c): HI-SCALE obs: 670.9.

398
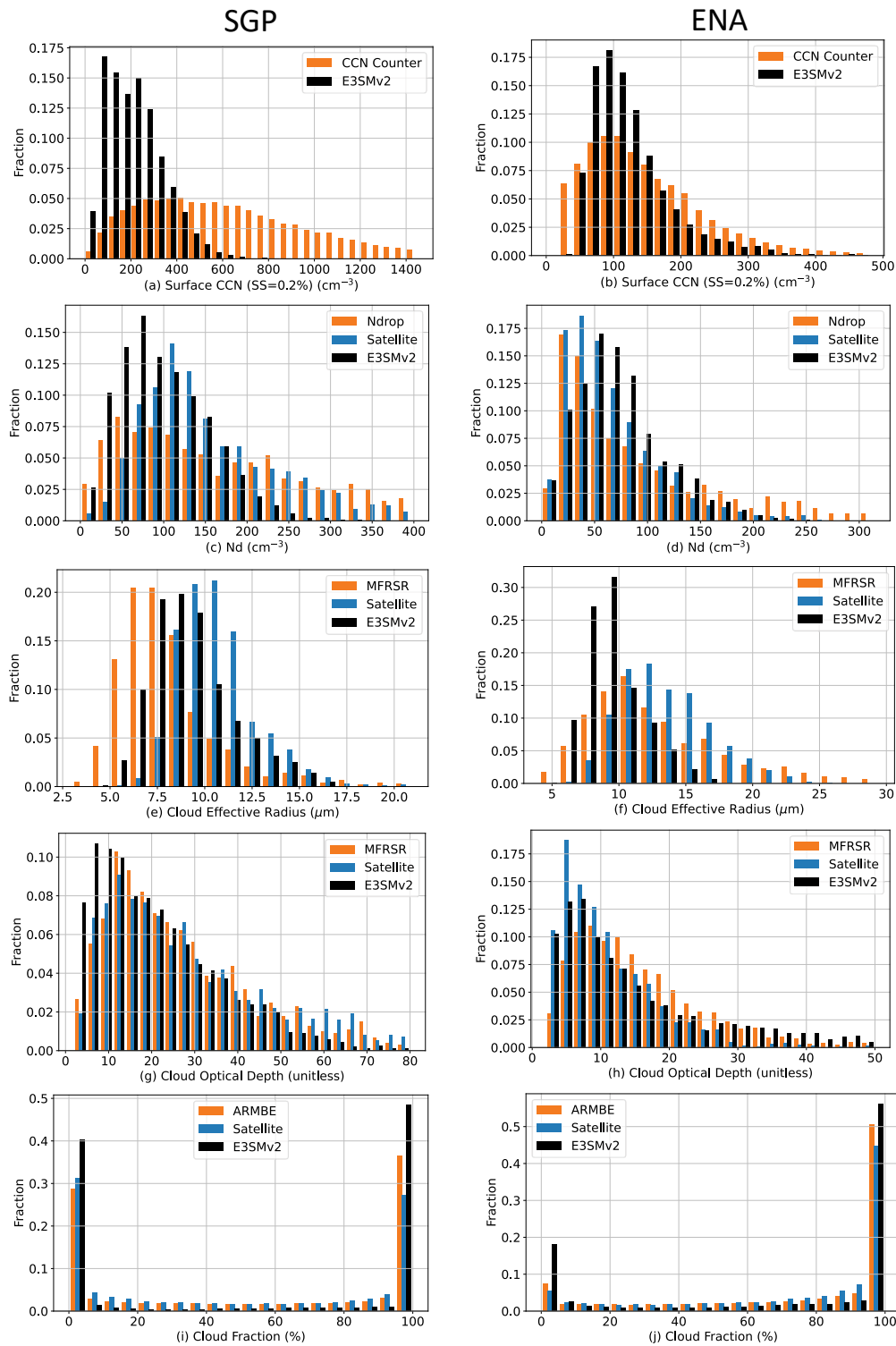
Figure 8: histogram of (from top to bottom) surface CCN number concentration, layer-mean N_d, R_{eff}, cloud optical depth and total cloud fraction at (left) SGP from 2011 to 2020 and (right) ENA from 2016 to 2018. Surface CCN and total cloud fraction are using all-condition samples while N_d, R_{eff}, cloud optical depth data are filtered for overcast

403 low-level liquid clouds (cloud top height < 4 km, cloud fraction > 90%, ice water path <
404 0.01 mm).

405 Figure 8 shows histograms of surface CCN number concentration in 0.2% supersaturation, cloud layer
406 mean N_d, R_{eff}, cloud optical depth and total cloud fraction for long-term diagnostics at SGP (year 2011-
407 2020) and ENA (year 2016-2018) sites. E3SMv2 fails to reproduce the long tail of large values in CCN
408 and N_d, especially over SGP. This is consistent with the underestimation of CN (> 100 nm) during the
409 HI-SCALE field campaign shown in Figures 6 and 7. Compared with ground retrievals, E3SMv2 R_{eff} is
410 larger at SGP but smaller at ENA. However, satellite-retrieved R_{eff} has larger values than E3SMv2 at
411 SGP. As discussed before, discrepancies between satellite and ground retrievals can be substantial for
412 some locations and variables, and considering both in evaluating model performance gives a sense for
413 how uncertain comparisons are. E3SMv2 generally captures the histograms of cloud optical depth and
414 total cloud fraction, although it underestimates the frequency of partial-cloudy conditions and
415 overestimates the frequency of clear-sky and overcast conditions.

416
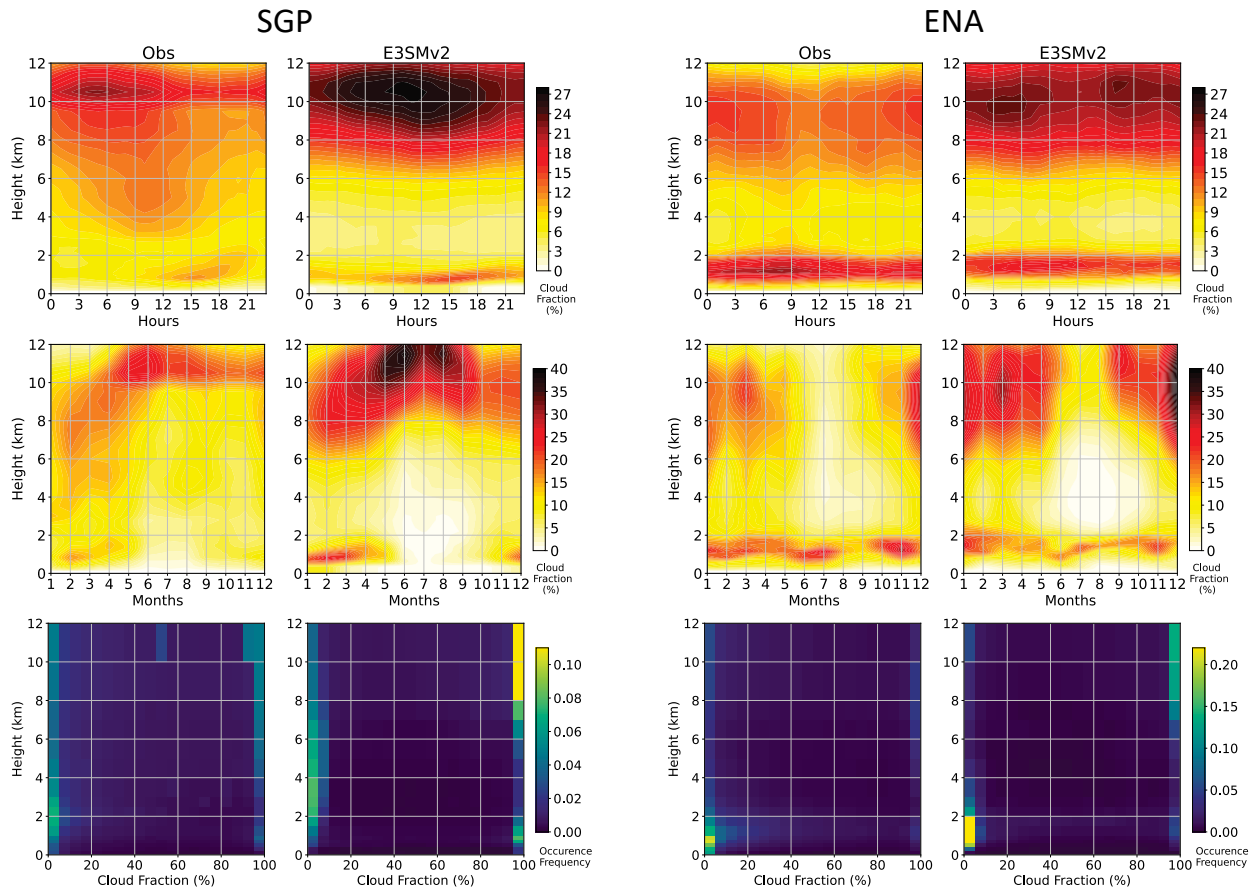
417

418 Figure 9: (top) Diurnal cycle, (middle) seasonal cycle, and (bottom) occurrence frequency
419 of vertical cloud fraction at (left) SGP from 2011 to 2020 and (right) ENA from 2016 to
420 2018.

421 Figure 9 shows the long-term diagnostics of mean diurnal cycles, seasonal cycles and histograms of cloud
422 fraction by height at SGP and ENA sites. Overall, the mean fraction of high clouds looks overestimated in
423 E3SMv2. Similar results has been reported in many previous studies in the Community Earth System
424 Model (CESM)-E3SM model family (e.g., Song et al., 2012; Cheng and Xu, 2013; Xu and Cheng, 2013b,
425 a; Tang et al., 2016; Zhang et al., 2020). However, this is not an apple-to-apple comparison, as cloud
426 fraction in ESMs includes clouds that are optically very thin that cannot be detected by satellite passive
427 sensors or cloud radars. The comparison of high cloud fraction from simulators with the corresponding
428 satellite observations showed that E3SM slightly underestimates high clouds over most tropical deep
429 convection regions (Zhang et al., 2019; Xie et al., 2018; Rasch et al., 2019). Unfortunately, ground-based
430 radar simulator of cloud vertical profiles is not available in the current model, which prevents a direct
431 apple-to-apple comparison. Thus, caution should be taken when comparing magnitude of cloud fraction
432 from direct model output and radar measurements. Here we focus on the temporal variabilities (diurnal
433 and seasonal cycles) and the occurrence frequency distribution of cloud fraction, which are less relevant
434 to the detection threshold of cloud radars.

435 At SGP, observations show formation of low clouds in the afternoon and in late winter through
436 springtime. High clouds peak overnight into the early morning and in the spring to summer,
437 corresponding to nocturnal deep convective systems common over SGP (Tang et al., 2022b; Tang et al.,
438 2021; Jiang et al., 2006). These features are reasonably well represented in E3SMv2, although low-level
439 cloud deepening in the afternoon is not well predicted, and high-level clouds peak in the late rather than
440 early morning. At ENA, marine stratus or stratocumulus clouds occur in any month and at any time of the
441 day, but with less frequency in late summer and in afternoon. High clouds are more frequent in winter
442 months than in summer months and occur throughout the diurnal cycle with a slight mid-day minimum.
443 These features are well captured by E3SMv2. At both sites, high clouds usually occur with high fraction
444 (> 95%) while low clouds are more likely associated with small fraction (< 5%) (bottom row). At SGP,
445 high occurrence of low cloud fraction extends vertically up to the tropopause, representing frequently
446 occurring deep convection. At ENA, low clouds have less vertical extension but are more likely to expand
447 to greater fraction. E3SMv2 reproduces these cloud features in occurrence frequency.

448   **5.2. Multi-variable relationships related to ACI**

449 The effective radiative forcing due to ACI processes are complex, nonlinear, and highly uncertain despite
450 their significant impact on climate. ACI studies are usually conducted by examining relationships
451 between aerosols, clouds, and radiation variables that are known to interact with one another. Given so
452 many variable combinations related to ACI, ESMAC Diags v2 provides a framework for users to examine
453 relationships between the variables they choose with joint histograms, scatter plots and heatmaps. Here
454 we show a few examples to assess relationships between CCN, N_d, LWP, and top of atmosphere (TOA)
455 albedo. ESMAC Diags v2 calculate layer-mean N_d from three sources: integrated vertically from native
456 model output, retrieved using Ndrop algorithm and using Nd_sat algorithm, as shown in Table 3. In this
457 study we only show the ACI diagnostics using native model output, as it reveals the "true" ACI relations
458 in the model. Users can choose to use the retrieved N_d in their studies for their purposes.

459 The dependence of TOA albedo on CCN number concentration for stratiform warm clouds can be
460 decomposed (e.g., following Quaas et al. (2008)) as:

461
$$\frac{dA}{dlnCCN} = \left(\frac{\partial A}{\partial lnN_d} + \frac{\partial A}{\partial lnLWP}\frac{dlnLWP}{dlnN_d}\right)\frac{dlnN_d}{dlnCCN} \qquad (1)$$

462   which allows isolation of "Twomey effect" $\left(\frac{\partial A}{\partial lnN_d}\right)\left(\frac{dlnN_d}{dlnCCN}\right)$ and "LWP adjustment" $\left(\frac{dlnLWP}{dlnN_d}\right)$ associated

463   with specific ACI processes. Here we use joint histograms and heatmaps to evaluate each component,

464   $\frac{dlnN_d}{dlnCCN}$, $\frac{dlnLWP}{dlnN_d}$, $\frac{\partial A}{\partial lnN_d}$ and $\frac{\partial A}{\partial lnLWP}$ based on long-term ground and satellite measurements at SGP (2011-

465   2020) and ENA (2016-2018) sites. The analysis in this section (except Figure 11) is limited to overcast

466   (cloud fraction > 90%), low-level (cloud top height < 4 km) liquid (ice water path < 0.01 mm) clouds.

467   Since there is no direct measurement of cloud base CCN concentration from remote sensors, surface CCN

468   concentration is used in this study and only clouds that are most likely to be affected by surface

469   conditions are examined. These clouds are identified as having cloud base potential temperature minus

470   surface potential temperature smaller than 2 K. For satellite measurements, samples with solar zenith

471   angle greater than 65° are removed to avoid N_d retrieval biases (Grosvenor et al., 2018). The sample

472   number of (ground, satellite, E3SM) for overcast low-level liquid clouds are (1766, 1217, 6369) at SGP

473   and (3450, 1345, 2884) at ENA, respectively. To increase sample size for more robust statistics, satellite

474   retrievals and E3SM outputs over a 5°×5° domain centered on SGP and ENA sites are included. This

475   increases the sample number to (1766, 71942, 15231) at SGP and (3450, 104260, 28184) at ENA.

476   Analyses of all-sky conditions and overcast low-level liquid clouds for a single grid point over each site

477   are shown in Figures S2-S7 in the supplementary material. Increasing sample domain for satellite and

478   E3SM data does not change the overall statistics shown here.

479   The change of N_d in response to a change of surface CCN number concentration $\left(\frac{dlnN_d}{dlnCCN}\right)$ is heavily

480   influenced by processes such as aerosol activation. Figure 10 shows the joint probability density function

481   (PDF)of N_d and surface CCN number concentration at 0.1% supersaturation normalized within each CCN

482   bin. Ground and satellite observations show similar linear fit of $lnN_d - lnCCN$ relation, although ground-

483   based plots have much smaller sample number. E3SMv2 shows more sensitive N_d – CCN relationships

484   than observations at both SGP and ENA sites, with the relationship tighter at ENA and more scattered at

485   SGP. As a cross validation, Figure 11 shows the N_d – CCN relationships from short-term aircraft

486   campaign during HI-SCALE and ACE-ENA. The comparison with in-situ aircraft measurements

487   confirms that E3SMv2 has more sensitive N_d to CCN relationship than observations. These results

488   indicate that aerosol activation in E3SMv2 may be too weak in low CCN conditions and too strong in

489   high CCN conditions, which may be related to the differences in simulated and observed updraft velocity

490   and supersaturation. Note that E3SMv2 produces a significant number of small N_d (< 20 cm^{-3}) samples

491   (Figure 11). This feature is reported in Golaz et al. (2022) and is partially removed by setting a minimum

492   threshold of $N_d = 10$ cm^{-3}. However, as seen in Figure 11, there are still a large number of N_d between 10

493   and 20 cm^{-3}. Further investigation is underway to diagnose the causes of the abundant low-N_d values. The

494   diagnostics shown here indicate that a more physical method should be applied to improve the simulated

495   N_d.

496
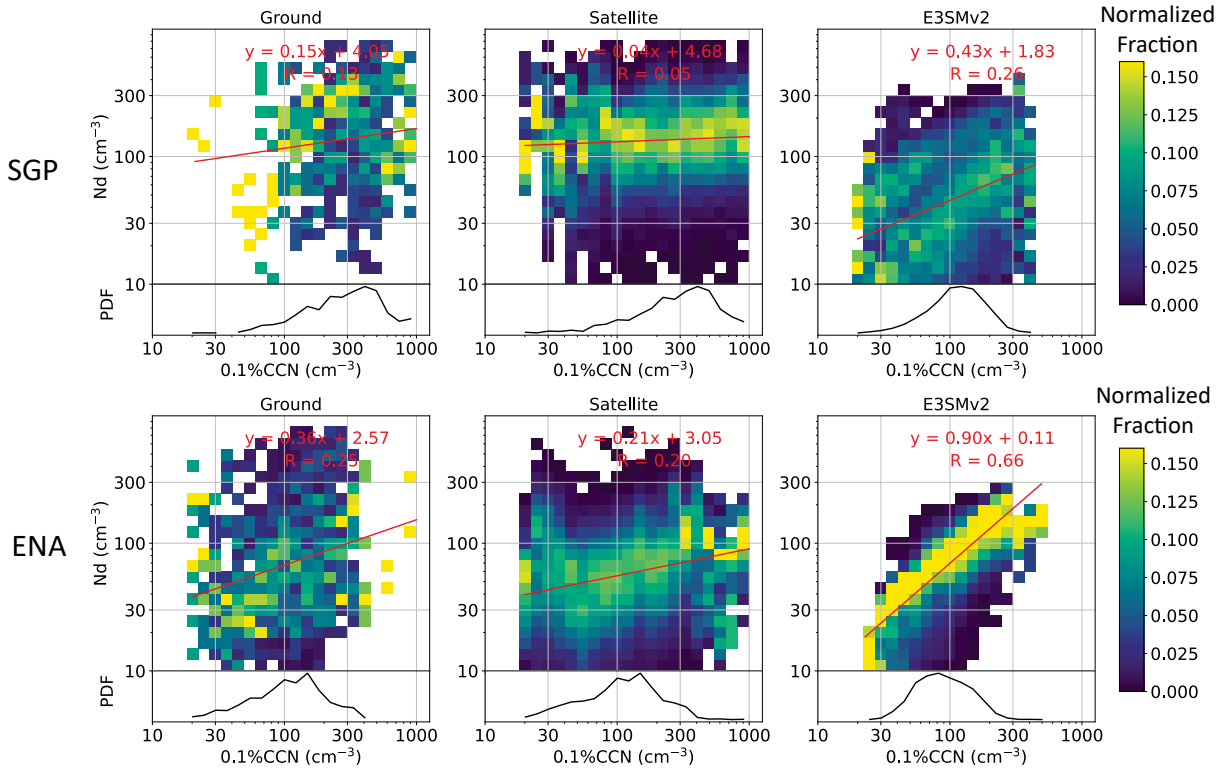
498 Figure 10: Joint histogram of layer-mean N_d versus surface CCN number concentration at
499 0.1% supersaturation, normalized within each CCN number concentration bin (PDF of
500 CCN shown in the bottom of each panel). Samples are constrained to likely surface-
501 coupled, overcast low-level liquid clouds (cloud top height < 4 km, cloud fraction > 90%,
502 ice water path < 0.01 mm and potential temperature difference between cloud base and
503 surface < 2 K). Available samples within a 5°×5° region centered on SGP (top) and ENA
504 (bottom) for satellite and E3SMv2 datasets are included. Linear fits and R values are
505 shown in red.
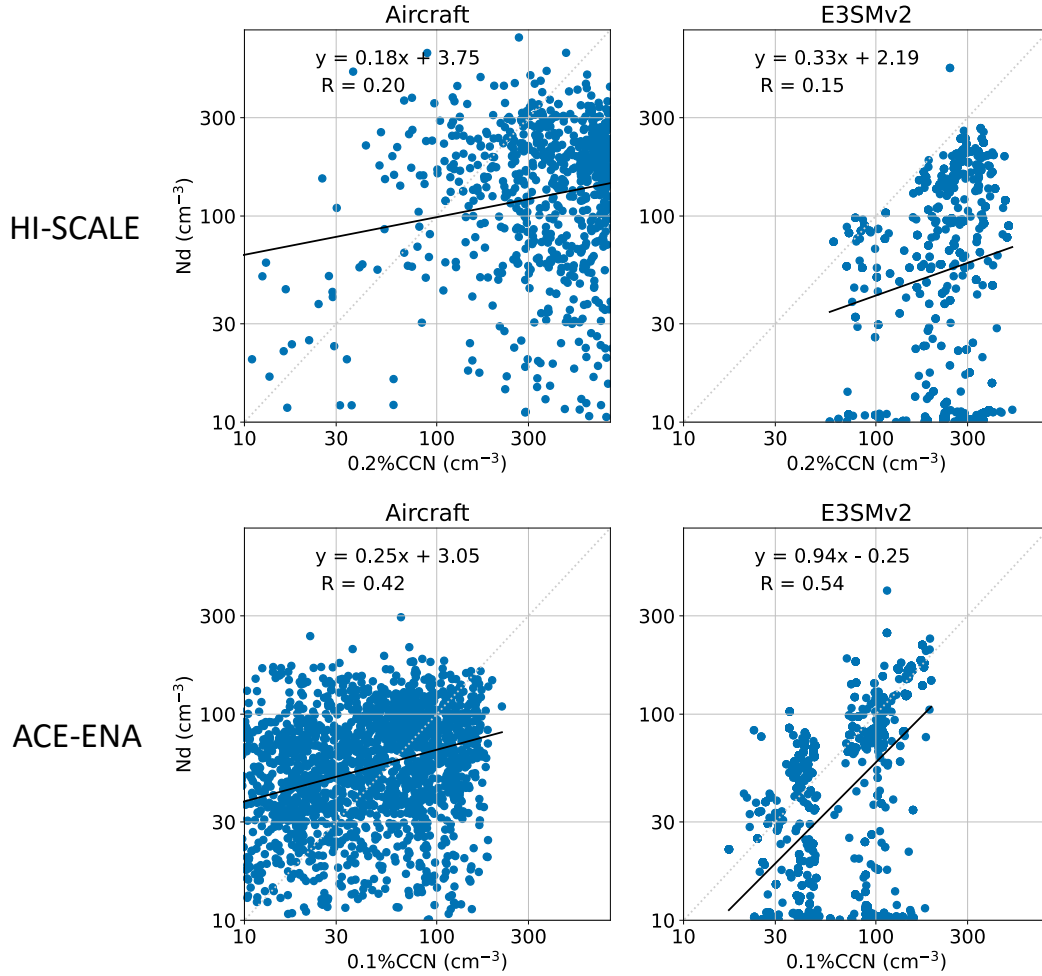
Figure 11: Scatter plots for N_d versus CCN along the flight tracks from (top) HI-SCALE and (bottom) ACE-ENA campaigns. Note that CCN number concentration measurements are taken under ~0.2% supersaturation for HI-SCALE and under ~0.1% supersaturation for ACE-ENA. Linear fits and R values are shown in each panel. R = 0.34 (SGP) and 0.74 (ENA) for E3SMv2 if a minimum N_d = 20 cm^{-3} is applied.

The term $\frac{dlnLWP}{dlnN_d}$ is commonly interpreted as the response of LWP to a perturbation in N_d tied to suppression of precipitation (increase LWP) or enhancement of evaporation (decrease LWP) (e.g., Glassmeier et al., 2019). Gryspeerdt et al. (2019) show that the satellite retrieved LWP over ocean increases with N_d when $N_d < \sim 30\ cm^{-3}$ and decreases when $N_d > \sim 30\ cm^{-3}$. This relation is also seen in satellite retrievals at ENA (Figure 12) when using a higher threshold $N_d = 50\ cm^{-3}$ to perform linear fits (black dashed lines). The linear fit is insignificant for $N_d < 50\ cm^{-3}$ in surface retrievals at both sites, partly due to small sample number, and also potentially related to drizzle contamination of LWP. The slope of the LWP – N_d relation in satellite retrievals at SGP is positive for both N_d ranges. This is opposed to the slope from the ground retrievals and satellite retrievals at ENA. This result reveals a few difficulties on LWP susceptibility studies based on observations. First, limitations of instruments and their

523 platforms (from space or from ground) employed in these observations as well as assumptions and
524 simplifications in their retrieval algorithms, may introduce biases and uncertainties into the retrieved
525 cloud microphysical properties. These biases and uncertainties can be amplified when studying ACI
526 relationships between multiple variables. Second, the robustness of ACI studies is also dependent on
527 geographical locations and cloud types, with environmental dynamic conditions influencing the analytical
528 outcomes. Despite our efforts to constrain meteorology and cloud situations, it is essential to
529 acknowledge the existence of many other factor, such as cloud adiabaticity and solar zenith angle as
530 discussed in Varble et al. (2023)), which can impact cloud susceptibility. Given these limitations and
531 uncertainties, researchers should use caution when using observational data to study ACI relationships.

532 The E3SMv2 simulated LWP – N_d relation is quite different from satellite retrievals at both sites. At
533 SGP, it generates a positive slope for $N_d < 50\ cm^{-3}$, and a negative slope for $N_d > 50\ cm^{-3}$. At ENA, it
534 shows an opposite relation, with LWP decreases for small N_d and increases for large N_d. The overall
535 LWP susceptibility in E3SMv2 is negative, which is consistent with observations and but differs from
536 most ESMs that produce a positive value (Quaas et al., 2009; Gryspeerdt et al., 2020). However, the
537 observed inverted "V" relation of LWP to Nd is oppositely seen in E3SMv2. We examined a few other
538 oceanic regions with frequent stratus or stratocumulus clouds and saw similar behavior (not shown). This
539 indicates possible different mechanisms of LWP susceptibility in E3SM than in observations. Our user-
540 friendly diagnostics package allows these analyses to be routinely performed for the purpose of better
541 understanding critical model behaviors at process- and mechanistic-levels, providing observational
542 constraints to facilitate model development efforts.

543

544
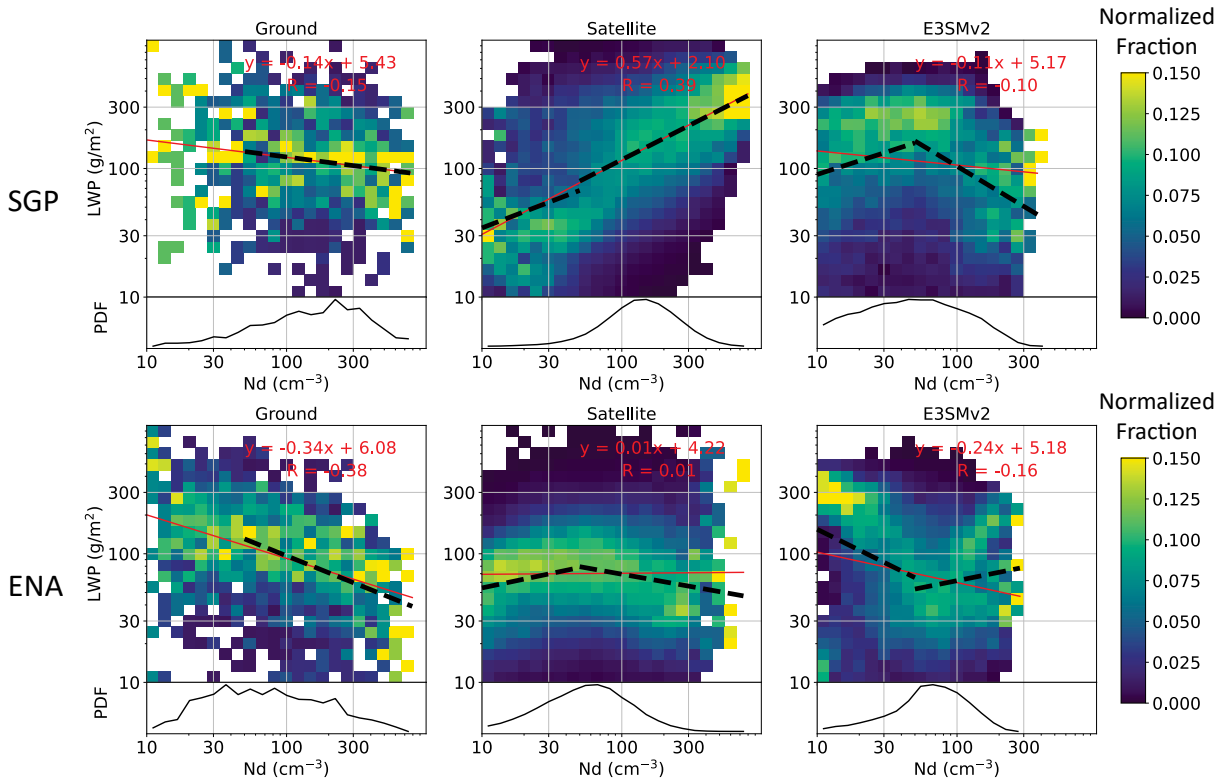
 Figure 12: Following Figure 10, but for the N_d bin-normalized joint histogram of LWP
546 versus N_d. Red lines and equations are linear fits for all data samples and black dashed
547 lines are linear fits for $N_d < 50\ cm^{-3}$ and $N_d > 50\ cm^{-3}$ when the fits are statistically
548 significant (p < 0.01).
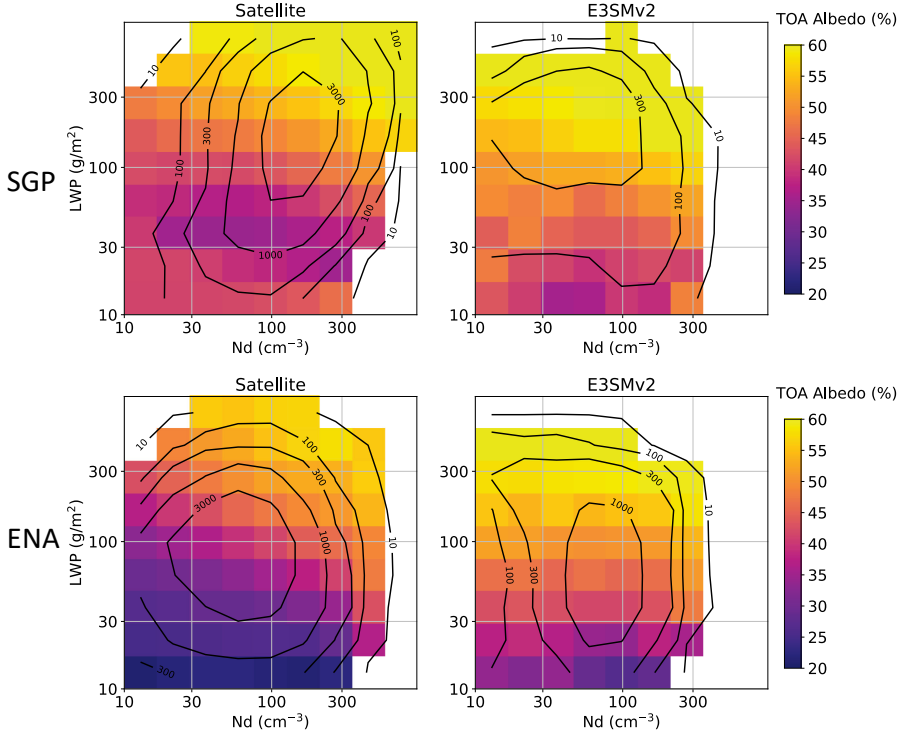
549

550 Figure 13: Heatmaps of mean TOA albedo versus LWP and N_d for likely surface-coupled,
551 overcast low-level liquid clouds (cloud top height < 4 km, cloud fraction > 90%, ice water
552 path < 0.01 mm and potential temperature difference between cloud base and surface < 2
553 K). Data include samples within a 5°×5° region centered on SGP (top) and ENA (bottom).
554 Valid sample number is shown in black contour lines. Grids with valid sample number <
555 10 are not filled. Ground data is not included, since the TOA albedo is not available.

556 Figure 13 shows heatmaps of mean TOA albedo with respect to LWP and N_d from which $\frac{\partial A}{\partial lnN_d}$ and
557 $\frac{\partial A}{\partial lnLWP}$ can be derived. At both ENA and SGP, TOA albedo generally increases with increases of LWP
558 and N_d, except at SGP when LWP is small. The increasing albedo in small LWP may be due to retrieval
559 artifact as uncertainty becomes large when LWP is small (e.g., < 20 g/m²), solar zenith angle is large
560 (e.g., > 55°), or cloud optical depth is small (e.g., <5) (Grosvenor et al., 2018). In most LWP-N_d bins,
561 TOA albedo at SGP is generally higher than at ENA, which is expected for clouds with smaller droplet
562 sizes. Increasing TOA albedo with increases of LWP is also seen in E3SMv2, but the dependence with N_d
563 is weak. This can be impacted by correlation between solar zenith angle and N_d in E3SM simulation, as
564 discussed in Varble et al. (2023). For a given LWP and N_d, TOA albedo is generally higher in E3SMv2
565 than in satellite observations, indicating that shallow clouds may be too reflective in the model, possibly
566 due to smaller cloud R_{eff} (Figure 8).

567 The above illustration of single-variable and multi-variable diagnostics present examples to demonstrate
568 the capability of ESMAC Diags v2. More analyses, such as selecting other variables, performing
569 additional data filtering or treatments, and examining ACI relationships with other variable combinations,
570 can be conducted through user-specified settings. A detailed user guide and a collection of example
571 scripts are included in the diagnostics package to assist users design customized diagnostics suited to their
572 specific needs.

573 **5. Summary**

574 We developed the Earth System Model aerosol-cloud diagnostics package (ESMAC Diags) to facilitate
575 routine evaluation of aerosols, clouds and ACI in the U.S. DOE's E3SM model using multiple platforms
576 of observations. As an updated version of ESMAC Diags v1 (Tang et al., 2022a) which mainly focuses on
577 aerosol properties, this paper described ESMAC Diags v2 that focuses on both aerosols, clouds, as well as
578 their interactions. In addition to the short-term field campaigns included in ESMAC Diags v1, long-term
579 diagnostics from two permanent ARM sites (SGP and ENA, each represents continental and maritime
580 conditions, respectively) are now conducted to provide more robust evaluation. The newly added multi-
581 variable joint histograms, scatter plots and heatmaps allow users to examine correlations between
582 variables that are relevant to the study of ACI.

583 Ground- and ship-based aerosol measurements are frequently impacted by local-scale emissions sources
584 such as those from airport or ship exhaust. These local sources are not resolved by coarse-resolution
585 ESMs, which usually represent an environment averaged within a region of tens to hundreds of kilometers
586 in size. In ESMAC Diags, we used available contamination-removed aerosol data, such as those from
587 Gallo et al. (2020) for ENA, and Humphries (2020) for MARCUS, and applied data filtering for other
588 field campaigns. The observations are harmonized into a uniform data format and temporal resolution that
589 are comparable with ESMs. Aircraft measurements retain higher resolution (currently 1-min) to preserve
590 high spatiotemporal variability, although ESMs have to be downscaled for evaluation with aircraft
591 measurements. This limitation of scale mismatch must be accepted to perform evaluation in current
592 coarse-resolution ESMs. Nevertheless, as ESM grid spacing approaches a few kilometers via regional
593 refinement (Tang et al., 2019) or global convection-permitting configuration (Caldwell et al., 2021), the
594 scale inconsistency between models and observations is reduced. ESMAC Diags can easily adjust the
595 preprocessing output resolution to facilitate the evaluation of high-resolution model output.

596 Cloud microphysical properties heavily rely on remote sensing measurements to achieve more robust
597 sampling, with imperfect retrieval algorithms needed to estimate these variables. Microphysical retrievals
598 are more uncertain than typical atmospheric state measurements due to the need for many assumptions
599 related to cloud dynamical and physical processes. We have shown (in Section 3) that ground- and
600 satellite-based retrievals of N_d and R_{eff} are overall consistent with each other and with in-situ aircraft
601 measurements, with some systematic differences such as smaller N_d and larger R_{eff} in satellite retrievals.
602 The discrepancies between different retrievals can be larger for individual days (e.g., Figure S1) but can
603 be mitigated to some degrees when considering broader statistics (Figures 3 and 4). The usage of multiple
604 retrieval datasets is critical to understand the robustness of evaluation results, as the spread between
605 different datasets indicates how robust model-observation differences are and guides interpretations of
606 model biases to support model development.

Finally, this paper presents a few examples of how well E3SMv2 simulates aerosols, clouds and ACI. We showed that ESMAC Diags can be used to target further investigation into specific parameterization components. For example, the analysis of N_d – CCN correlation indicates that E3SMv2 may exhibit too weak aerosol activation in low CCN conditions and too strong in high CCN conditions; the analysis of $LWP – N_d$ correlation indicates that either the precipitation suppression and cloud evaporation mechanisms are not well represented, or there are other mechanisms dominating $LWP – N_d$ correlation in E3SMv2. These diagnostic analyses provide insights into areas in aerosols, clouds and ACI that warrant special attention in future model development efforts. As ESMs continuously improve its physical parameterizations, resolution, and numerical schemes, ESMAC Diags offers a valuable tool for systematically evaluating the performance of the newer versions of a model in simulating aerosol, clouds and ACI.

618 **Code availability**:

619 *The current version of ESMAC Diags is publicly available through GitHub (https://github.com/eagles-*
620 *project/ESMAC_diags) under the new BSD license. The exact version (2.1.2) of the code used to produce*
621 *the results used in this paper is archived on Zenodo (https://doi.org/10.5281/zenodo.7696871). The model*
622 *simulation used in this paper is version 2.0 (https://doi.org/10.11578/E3SM/dc.20210927.1) of E3SM.*

623 **Data availability**:

624 *Measurements from the HI-SCALE, ACE-ENA, MAGIC, and MARCUS campaigns as well as the SGP*
625 *and ENA sites are supported by the DOE Atmospheric Radiation Measurement (ARM) user facility and*
626 *available at https://adc.arm.gov/discovery/. Measurements from the CSET and SOCRATES campaigns*
627 *are supported by National Science Foundation (NSF) and obtained from NCAR Earth Observing*
628 *Laboratory at https://data.eol.ucar.edu/master_lists/generated/cset/ and*
629 *https://data.eol.ucar.edu/master_lists/generated/socrates/, respectively. DOI numbers or references of*
630 *individual datasets are given in Tables S1-S8. All the preprocessed observational and model data used to*
631 *produce the results used in this paper is archived on Zenodo (https://doi.org/10.5281/zenodo.7478657).*

632 **Author contribution**:

633 *ST, JDF and PM designed the diagnostics package; ST and ACV wrote the code and performed the*
634 *analysis; PW, XD, FM and MP processed the field campaign datasets and provided discussions on the*
635 *data quality issues; KZ contributed to the model simulation; JCH contributed to the package design and*
636 *setup; ST wrote the original manuscript; all authors reviewed and edited the manuscript.*

637 **Competing interests**:

638 *Po-Lun Ma is a Topical Editor of Geoscientific Model Development. Other authors declare that they have*
639 *no conflict of interest.*

640 *Acknowledgements:*

641 *This study was supported by the Enabling Aerosol-cloud interactions at GLobal convection-permitting*
642 *scalES (EAGLES) project (74358), funded by the U.S. Department of Energy, Office of Science, Office of*
643 *Biological and Environmental Research, Earth System Model Development (ESMD) program area. We*
644 *thank the numerous instrument mentors for providing the data. This research used resources of the*
645 *National Energy Research Scientific Computing Center (NERSC), a U.S. Department of Energy Office of*
646 *Science User Facility operated under Contract No. DE-AC02-05CH11231, using NERSC awards ALCC-*
647 *ERCAP0016315, BER-ERCAP0015329, BER-ERCAP0018473, and BER-ERCAP0020990. Pacific*
648 *Northwest National Laboratory (PNNL) is operated for DOE by Battelle Memorial Institute under*
649 *contract DE-AC05-76RL01830.*

650

651 **References**:

652 Albrecht, B., Ghate, V., Mohrmann, J., Wood, R., Zuidema, P., Bretherton, C., Schwartz, C., Eloranta, E.,
653 Glienke, S., Donaher, S., Sarkar, M., McGibbon, J., Nugent, A. D., Shaw, R. A., Fugal, J., Minnis, P.,
654 Paliknoda, R., Lussier, L., Jensen, J., Vivekanandan, J., Ellis, S., Tsai, P., Rilling, R., Haggerty, J.,
655 Campos, T., Stell, M., Reeves, M., Beaton, S., Allison, J., Stossmeister, G., Hall, S., and Schmidt, S.:
656 Cloud System Evolution in the Trades (CSET): Following the Evolution of Boundary Layer Cloud
657 Systems with the NSF–NCAR GV, Bull. Amer. Meteor. Soc., 100, 93-121, 10.1175/bams-d-17-0180.1,
658 2019.

659 AMWG Diagnostic Package: https://www.cesm.ucar.edu/working_groups/Atmosphere/amwg-
660 diagnostics-package/, last access: 2 November 2021.

661 Bennartz, R.: Global assessment of marine boundary layer cloud droplet number concentration from
662 satellite, Journal of Geophysical Research: Atmospheres, 112, 10.1029/2006JD007547, 2007.

663 Caldwell, P. M., Terai, C. R., Hillman, B., Keen, N. D., Bogenschutz, P., Lin, W., Beydoun, H., Taylor,
664 M., Bertagna, L., Bradley, A. M., Clevenger, T. C., Donahue, A. S., Eldred, C., Foucar, J., Golaz, J.-C.,
665 Guba, O., Jacob, R., Johnson, J., Krishna, J., Liu, W., Pressel, K., Salinger, A. G., Singh, B., Steyer, A.,
666 Ullrich, P., Wu, D., Yuan, X., Shpund, J., Ma, H.-Y., and Zender, C. S.: Convection-Permitting
667 Simulations With the E3SM Global Atmosphere Model, Journal of Advances in Modeling Earth Systems,
668 13, e2021MS002544, 10.1029/2021MS002544, 2021.

669 Cheng, A. and Xu, K.-M.: Evaluating Low-Cloud Simulation from an Upgraded Multiscale Modeling
670 Framework Model. Part III: Tropical and Subtropical Cloud Transitions over the Northern Pacific, J.
671 Climate, 26, 5761-5781, 10.1175/JCLI-D-12-00650.1, 2013.

672 Choudhury, G. and Tesche, M.: Estimating cloud condensation nuclei concentrations from CALIPSO
673 lidar measurements, Atmos. Meas. Tech., 15, 639-654, 10.5194/amt-15-639-2022, 2022.

674 E3SM Diagnostics: https://e3sm.org/resources/tools/diagnostic-tools/e3sm-diagnostics/, last access: 2
675 November 2021.

676 Eyring, V., Righi, M., Lauer, A., Evaldsson, M., Wenzel, S., Jones, C., Anav, A., Andrews, O., Cionni, I.,
677 Davin, E. L., Deser, C., Ehbrecht, C., Friedlingstein, P., Gleckler, P., Gottschaldt, K. D., Hagemann, S.,
678 Juckes, M., Kindermann, S., Krasting, J., Kunert, D., Levine, R., Loew, A., Mäkelä, J., Martin, G.,
679 Mason, E., Phillips, A. S., Read, S., Rio, C., Roehrig, R., Senftleben, D., Sterl, A., van Ulft, L. H.,
680 Walton, J., Wang, S., and Williams, K. D.: ESMValTool (v1.0) – a community diagnostic and
681 performance metrics tool for routine evaluation of Earth system models in CMIP, Geosci. Model Dev., 9,
682 1747-1802, 10.5194/gmd-9-1747-2016, 2016.

683 Fast, J. D., Berg, L. K., Alexander, L., Bell, D., D'Ambro, E., Hubbe, J., Kuang, C., Liu, J., Long, C.,
684 Matthews, A., Mei, F., Newsom, R., Pekour, M., Pinterich, T., Schmid, B., Schobesberger, S., Shilling, J.,
685 Smith, J. N., Springston, S., Suski, K., Thornton, J. A., Tomlinson, J., Wang, J., Xiao, H., and Zelenyuk,
686 A.: Overview of the HI-SCALE Field Campaign: A New Perspective on Shallow Convective Clouds,
687 Bull. Amer. Meteor. Soc., 100, 821-840, 10.1175/bams-d-18-0030.1, 2019.

688 Gallo, F., Uin, J., Springston, S., Wang, J., Zheng, G., Kuang, C., Wood, R., Azevedo, E. B.,
689 McComiskey, A., Mei, F., Theisen, A., Kyrouac, J., and Aiken, A. C.: Identifying a regional aerosol
690 baseline in the eastern North Atlantic using collocated measurements and a mathematical algorithm to
691 mask high-submicron-number-concentration aerosol events, Atmos. Chem. Phys., 20, 7553-7573,
692 10.5194/acp-20-7553-2020, 2020.

693 Gelaro, R., McCarty, W., Suarez, M. J., Todling, R., Molod, A., Takacs, L., Randles, C., Darmenov, A.,
694 Bosilovich, M. G., Reichle, R., Wargan, K., Coy, L., Cullather, R., Draper, C., Akella, S., Buchard, V.,
695 Conaty, A., da Silva, A., Gu, W., Kim, G. K., Koster, R., Lucchesi, R., Merkova, D., Nielsen, J. E.,

Partyka, G., Pawson, S., Putman, W., Rienecker, M., Schubert, S. D., Sienkiewicz, M., and Zhao, B.: The Modern-Era Retrospective Analysis for Research and Applications, Version 2 (MERRA-2), J. Climate, 30, 5419-5454, 10.1175/JCLI-D-16-0758.1, 2017.

Glassmeier, F., Hoffmann, F., Johnson, J. S., Yamaguchi, T., Carslaw, K. S., and Feingold, G.: An emulator approach to stratocumulus susceptibility, Atmos. Chem. Phys., 19, 10191-10203, 10.5194/acp-19-10191-2019, 2019.

Gleckler, P. J., Doutriaux, C., Durack, P. J., Taylor, K. E., Zhang, Y., Williams, D. N., Mason, E., and Servonnat, J.: A more powerful reality test for climate models, Eos, Trans. Amer. Geophys. Union, 97, 10.1029/2016EO051663, 2016.

Golaz, J.-C., Van Roekel, L. P., Zheng, X., Roberts, A. F., Wolfe, J. D., Lin, W., Bradley, A. M., Tang, Q., Maltrud, M. E., Forsyth, R. M., Zhang, C., Zhou, T., Zhang, K., Zender, C. S., Wu, M., Wang, H., Turner, A. K., Singh, B., Richter, J. H., Qin, Y., Petersen, M. R., Mametjanov, A., Ma, P.-L., Larson, V. E., Krishna, J., Keen, N. D., Jeffery, N., Hunke, E. C., Hannah, W. M., Guba, O., Griffin, B. M., Feng, Y., Engwirda, D., Di Vittorio, A. V., Dang, C., Conlon, L. M., Chen, C.-C.-J., Brunke, M. A., Bisht, G., Benedict, J. J., Asay-Davis, X. S., Zhang, Y., Zhang, M., Zeng, X., Xie, S., Wolfram, P. J., Vo, T., Veneziani, M., Tesfa, T. K., Sreepathi, S., Salinger, A. G., Jack Reeves Eyre, J. E., Prather, M. J., Mahajan, S., Li, Q., Jones, P. W., Jacob, R. L., Huebler, G. W., Huang, X., Hillman, B. R., Harrop, B. E., Foucar, J. G., Fang, Y., Comeau, D. S., Caldwell, P. M., Bartoletti, T., Balaguru, K., Taylor, M. A., McCoy, R. B., Leung, L. R., and Bader, D. C.: The DOE E3SM Model Version 2: Overview of the physical model and initial model evaluation, Journal of Advances in Modeling Earth Systems, n/a, e2022MS003156, 10.1029/2022MS003156, 2022.

Golaz, J.-C., Caldwell, P. M., Van Roekel, L. P., Petersen, M. R., Tang, Q., Wolfe, J. D., Abeshu, G., Anantharaj, V., Asay-Davis, X. S., Bader, D. C., Baldwin, S. A., Bisht, G., Bogenschutz, P. A., Branstetter, M., Brunke, M. A., Brus, S. R., Burrows, S. M., Cameron-Smith, P. J., Donahue, A. S., Deakin, M., Easter, R. C., Evans, K. J., Feng, Y., Flanner, M., Foucar, J. G., Fyke, J. G., Griffin, B. M., Hannay, C., Harrop, B. E., Hoffman, M. J., Hunke, E. C., Jacob, R. L., Jacobsen, D. W., Jeffery, N., Jones, P. W., Keen, N. D., Klein, S. A., Larson, V. E., Leung, L. R., Li, H.-Y., Lin, W., Lipscomb, W. H., Ma, P.-L., Mahajan, S., Maltrud, M. E., Mametjanov, A., McClean, J. L., McCoy, R. B., Neale, R. B., Price, S. F., Qian, Y., Rasch, P. J., Reeves Eyre, J. E. J., Riley, W. J., Ringler, T. D., Roberts, A. F., Roesler, E. L., Salinger, A. G., Shaheen, Z., Shi, X., Singh, B., Tang, J., Taylor, M. A., Thornton, P. E., Turner, A. K., Veneziani, M., Wan, H., Wang, H., Wang, S., Williams, D. N., Wolfram, P. J., Worley, P. H., Xie, S., Yang, Y., Yoon, J.-H., Zelinka, M. D., Zender, C. S., Zeng, X., Zhang, C., Zhang, K., Zhang, Y., Zheng, X., Zhou, T., and Zhu, Q.: The DOE E3SM Coupled Model Version 1: Overview and Evaluation at Standard Resolution, J. Adv. Model. Earth Syst., 11, 2089-2129, 10.1029/2018ms001603, 2019.

Grosvenor, D. P., Sourdeval, O., Zuidema, P., Ackerman, A., Alexandrov, M. D., Bennartz, R., Boers, R., Cairns, B., Chiu, J. C., Christensen, M., Deneke, H., Diamond, M., Feingold, G., Fridlind, A., Hünerbein, A., Knist, C., Kollias, P., Marshak, A., McCoy, D., Merk, D., Painemal, D., Rausch, J., Rosenfeld, D., Russchenberg, H., Seifert, P., Sinclair, K., Stier, P., van Diedenhoven, B., Wendisch, M., Werner, F., Wood, R., Zhang, Z., and Quaas, J.: Remote Sensing of Droplet Number Concentration in Warm Clouds: A Review of the Current State of Knowledge and Perspectives, Reviews of Geophysics, 56, 409-453, 10.1029/2017RG000593, 2018.

Gryspeerdt, E., Goren, T., Sourdeval, O., Quaas, J., Mülmenstädt, J., Dipu, S., Unglaub, C., Gettelman, A., and Christensen, M.: Constraining the aerosol influence on cloud liquid water path, Atmos. Chem. Phys., 19, 5331-5347, 10.5194/acp-19-5331-2019, 2019.

Gryspeerdt, E., Mülmenstädt, J., Gettelman, A., Malavelle, F. F., Morrison, H., Neubauer, D., Partridge, D. G., Stier, P., Takemura, T., Wang, H., Wang, M., and Zhang, K.: Surprising similarities in model and

observational aerosol radiative forcing estimates, Atmos. Chem. Phys., 20, 613-623, 10.5194/acp-20-613-2020, 2020.

Humphries, R.: MARCUS ARM CN and CCN data reprocessed to remove ship exhaust influence (v2) [dataset], 10.25919/ezp0-em87, 2020.

Humphries, R. S., McRobert, I. M., Ponsonby, W. A., Ward, J. P., Keywood, M. D., Loh, Z. M., Krummel, P. B., and Harnwell, J.: Identification of platform exhaust on the RV Investigator, Atmos. Meas. Tech., 12, 3019-3038, 10.5194/amt-12-3019-2019, 2019.

IPCC: Climate Change 2021: The Physical Science Basis. Contribution of Working Group I to the Sixth Assessment Report of the Intergovernmental Panel on Climate Change, Cambridge University Press, Cambridge, United Kingdom and New York, NY, USA, 2391 pp., 10.1017/9781009157896, 2021.

Jiang, X., Lau, N.-C., and Klein, S. A.: Role of eastward propagating convection systems in the diurnal cycle and seasonal mean of summertime rainfall over the U.S. Great Plains, Geophys. Res. Lett., 33, 10.1029/2006gl027022, 2006.

Lewis, E. R. and Teixeira, J.: Dispelling clouds of uncertainty, Eos, Trans. Amer. Geophys. Union, 96, 10.1029/2015eo031303, 2015.

Lim, K.-S. S., Riihimaki, L., Comstock, J. M., Schmid, B., Sivaraman, C., Shi, Y., and McFarquhar, G. M.: Evaluation of long-term surface-retrieved cloud droplet number concentration with in situ aircraft observations, Journal of Geophysical Research: Atmospheres, 121, 2318-2331, 10.1002/2015JD024082, 2016.

Ma, P. L., Harrop, B. E., Larson, V. E., Neale, R. B., Gettelman, A., Morrison, H., Wang, H., Zhang, K., Klein, S. A., Zelinka, M. D., Zhang, Y., Qian, Y., Yoon, J. H., Jones, C. R., Huang, M., Tai, S. L., Singh, B., Bogenschutz, P. A., Zheng, X., Lin, W., Quaas, J., Chepfer, H., Brunke, M. A., Zeng, X., Mülmenstädt, J., Hagos, S., Zhang, Z., Song, H., Liu, X., Pritchard, M. S., Wan, H., Wang, J., Tang, Q., Caldwell, P. M., Fan, J., Berg, L. K., Fast, J. D., Taylor, M. A., Golaz, J. C., Xie, S., Rasch, P. J., and Leung, L. R.: Better calibration of cloud parameterizations and subgrid effects increases the fidelity of the E3SM Atmosphere Model version 1, Geosci. Model Dev., 15, 2881-2916, 10.5194/gmd-15-2881-2022, 2022.

Maloney, E. D., Gettelman, A., Ming, Y., Neelin, J. D., Barrie, D., Mariotti, A., Chen, C. C., Coleman, D. R. B., Kuo, Y.-H., Singh, B., Annamalai, H., Berg, A., Booth, J. F., Camargo, S. J., Dai, A., Gonzalez, A., Hafner, J., Jiang, X., Jing, X., Kim, D., Kumar, A., Moon, Y., Naud, C. M., Sobel, A. H., Suzuki, K., Wang, F., Wang, J., Wing, A. A., Xu, X., and Zhao, M.: Process-Oriented Evaluation of Climate and Weather Forecasting Models, Bull. Amer. Meteor. Soc., 100, 1665-1686, 10.1175/bams-d-18-0042.1, 2019.

McFarquhar, G. M., Bretherton, C. S., Marchand, R., Protat, A., DeMott, P. J., Alexander, S. P., Roberts, G. C., Twohy, C. H., Toohey, D., Siems, S., Huang, Y., Wood, R., Rauber, R. M., Lasher-Trapp, S., Jensen, J., Stith, J. L., Mace, J., Um, J., Järvinen, E., Schnaiter, M., Gettelman, A., Sanchez, K. J., McCluskey, C. S., Russell, L. M., McCoy, I. L., Atlas, R. L., Bardeen, C. G., Moore, K. A., Hill, T. C. J., Humphries, R. S., Keywood, M. D., Ristovski, Z., Cravigan, L., Schofield, R., Fairall, C., Mallet, M. D., Kreidenweis, S. M., Rainwater, B., D'Alessandro, J., Wang, Y., Wu, W., Saliba, G., Levin, E. J. T., Ding, S., Lang, F., Truong, S. C. H., Wolff, C., Haggerty, J., Harvey, M. J., Klekociuk, A. R., and McDonald, A.: Observations of Clouds, Aerosols, Precipitation, and Surface Radiation over the Southern Ocean: An Overview of CAPRICORN, MARCUS, MICRE, and SOCRATES, Bull. Amer. Meteor. Soc., 102, E894-E928, 10.1175/bams-d-20-0132.1, 2021.

Min, Q. and Harrison, L. C.: Cloud properties derived from surface MFRSR measurements and comparison with GOES results at the ARM SGP Site, Geophysical Research Letters, 23, 1641-1644, 10.1029/96GL01488, 1996.

Minnis, P., Nguyen, L., Palikonda, R., Heck, P. W., Spangenberg, D. A., Doelling, D. R., Ayers, J. K., Smith, J. W. L., Khaiyer, M. M., Trepte, Q. Z., Avey, L. A., Chang, F.-L., Yost, C. R., Chee, T. L., and Szedung, S.-M.: Near-real time cloud retrievals from operational and research meteorological satellites, Proc. SPIE Europe Remote Sens., Cardiff, Wales, UK,, 15-18 September, 710703, 10.1117/12.800344, 2008.

Minnis, P., Sun-Mack, S., Young, D. F., Heck, P. W., Garber, D. P., Chen, Y., Spangenberg, D. A., Arduini, R. F., Trepte, Q. Z., Smith, W. L., Ayers, J. K., Gibson, S. C., Miller, W. F., Hong, G., Chakrapani, V., Takano, Y., Liou, K. N., Xie, Y., and Yang, P.: CERES Edition-2 Cloud Property Retrievals Using TRMM VIRS and Terra and Aqua MODIS Data—Part I: Algorithms, IEEE Transactions on Geoscience and Remote Sensing, 49, 4374-4400, 10.1109/TGRS.2011.2144601, 2011.

Myhre, G., Samset, B. H., Schulz, M., Balkanski, Y., Bauer, S., Berntsen, T. K., Bian, H., Bellouin, N., Chin, M., Diehl, T., Easter, R. C., Feichter, J., Ghan, S. J., Hauglustaine, D., Iversen, T., Kinne, S., Kirkevåg, A., Lamarque, J. F., Lin, G., Liu, X., Lund, M. T., Luo, G., Ma, X., van Noije, T., Penner, J. E., Rasch, P. J., Ruiz, A., Seland, Ø., Skeie, R. B., Stier, P., Takemura, T., Tsigaridis, K., Wang, P., Wang, Z., Xu, L., Yu, H., Yu, F., Yoon, J. H., Zhang, K., Zhang, H., and Zhou, C.: Radiative forcing of the direct aerosol effect from AeroCom Phase II simulations, Atmos. Chem. Phys., 13, 1853-1877, 10.5194/acp-13-1853-2013, 2013.

NETCDF: Introduction and Overview: https://www.unidata.ucar.edu/software/netcdf/docs/index.html, last access: 12 November 2022.

Quaas, J., Boucher, O., Bellouin, N., and Kinne, S.: Satellite-based estimate of the direct and indirect aerosol climate forcing, Journal of Geophysical Research: Atmospheres, 113, 10.1029/2007JD008962, 2008.

Quaas, J., Ming, Y., Menon, S., Takemura, T., Wang, M., Penner, J. E., Gettelman, A., Lohmann, U., Bellouin, N., Boucher, O., Sayer, A. M., Thomas, G. E., McComiskey, A., Feingold, G., Hoose, C., Kristjánsson, J. E., Liu, X., Balkanski, Y., Donner, L. J., Ginoux, P. A., Stier, P., Grandey, B., Feichter, J., Sednev, I., Bauer, S. E., Koch, D., Grainger, R. G., Kirkev, aring, g, A., Iversen, T., Seland, Ø., Easter, R., Ghan, S. J., Rasch, P. J., Morrison, H., Lamarque, J. F., Iacono, M. J., Kinne, S., and Schulz, M.: Aerosol indirect effects – general circulation model intercomparison and evaluation with satellite data, Atmos. Chem. Phys., 9, 8697-8717, 10.5194/acp-9-8697-2009, 2009.

Rasch, P. J., Xie, S., Ma, P.-L., Lin, W., Wang, H., Tang, Q., Burrows, S. M., Caldwell, P., Zhang, K., Easter, R. C., Cameron-Smith, P., Singh, B., Wan, H., Golaz, J.-C., Harrop, B. E., Roesler, E., Bacmeister, J., Larson, V. E., Evans, K. J., Qian, Y., Taylor, M., Leung, L. R., Zhang, Y., Brent, L., Branstetter, M., Hannay, C., Mahajan, S., Mametjanov, A., Neale, R., Richter, J. H., Yoon, J.-H., Zender, C. S., Bader, D., Flanner, M., Foucar, J. G., Jacob, R., Keen, N., Klein, S. A., Liu, X., Salinger, A. G., Shrivastava, M., and Yang, Y.: An Overview of the Atmospheric Component of the Energy Exascale Earth System Model, J. Adv. Model. Earth Syst., 11, 2377-2411, 10.1029/2019ms001629, 2019.

Reddington, C. L., Carslaw, K. S., Stier, P., Schutgens, N., Coe, H., Liu, D., Allan, J., Browse, J., Pringle, K. J., Lee, L. A., Yoshioka, M., Johnson, J. S., Regayre, L. A., Spracklen, D. V., Mann, G. W., Clarke, A., Hermann, M., Henning, S., Wex, H., Kristensen, T. B., Leaitch, W. R., Pöschl, U., Rose, D., Andreae, M. O., Schmale, J., Kondo, Y., Oshima, N., Schwarz, J. P., Nenes, A., Anderson, B., Roberts, G. C., Snider, J. R., Leck, C., Quinn, P. K., Chi, X., Ding, A., Jimenez, J. L., and Zhang, Q.: The Global Aerosol Synthesis and Science Project (GASSP): Measurements and Modeling to Reduce Uncertainty, Bull. Amer. Meteor. Soc., 98, 1857-1877, 10.1175/bams-d-15-00317.1, 2017.

Riihimaki, L., McFarlane, S., and Sivaraman, C.: Droplet Number Concentration Value-Added Product, ARM Research FacilityDOE/SC-ARM-TR-140, 2021.

834 Schulz, M., Textor, C., Kinne, S., Balkanski, Y., Bauer, S., Berntsen, T., Berglen, T., Boucher, O.,
835 Dentener, F., Guibert, S., Isaksen, I. S. A., Iversen, T., Koch, D., Kirkevåg, A., Liu, X., Montanaro, V.,
836 Myhre, G., Penner, J. E., Pitari, G., Reddy, S., Seland, Ø., Stier, P., and Takemura, T.: Radiative forcing
837 by aerosols as derived from the AeroCom present-day and pre-industrial simulations, Atmos. Chem.
838 Phys., 6, 5225-5246, 10.5194/acp-6-5225-2006, 2006.

839 Song, X., Zhang, G. J., and Li, J. L. F.: Evaluation of Microphysics Parameterization for Convective
840 Clouds in the NCAR Community Atmosphere Model CAM5, J. Climate, 25, 8568-8590, 10.1175/JCLI-
841 D-11-00563.1, 2012.

842 Sun, J., Zhang, K., Wan, H., Ma, P.-L., Tang, Q., and Zhang, S.: Impact of Nudging Strategy on the
843 Climate Representativeness and Hindcast Skill of Constrained EAMv1 Simulations, J. Adv. Model. Earth
844 Syst., 11, 3911-3933, 10.1029/2019MS001831, 2019.

845 Tang, Q., Klein, S. A., Xie, S., Lin, W., Golaz, J. C., Roesler, E. L., Taylor, M. A., Rasch, P. J., Bader, D.
846 C., Berg, L. K., Caldwell, P., Giangrande, S. E., Neale, R. B., Qian, Y., Riihimaki, L. D., Zender, C. S.,
847 Zhang, Y., and Zheng, X.: Regionally refined test bed in E3SM atmosphere model version 1 (EAMv1)
848 and applications for high-resolution modeling, Geosci. Model Dev., 12, 2679-2706, 10.5194/gmd-12-
849 2679-2019, 2019.

850 Tang, S., Zhang, M., and Xie, S.: An ensemble constrained variational analysis of atmospheric forcing
851 data and its application to evaluate clouds in CAM5, J. Geophys. Res. Atmos., 121, 33-48,
852 10.1002/2015JD024167, 2016.

853 Tang, S., Gleckler, P., Xie, S., Lee, J., Ahn, M.-S., Covey, C., and Zhang, C.: Evaluating the Diurnal and
854 Semidiurnal Cycle of Precipitation in CMIP6 Models Using Satellite- and Ground-Based Observations, J.
855 Climate, 34, 3189-3210, 10.1175/jcli-d-20-0639.1, 2021.

856 Tang, S., Fast, J. D., Zhang, K., Hardin, J. C., Varble, A. C., Shilling, J. E., Mei, F., Zawadowicz, M. A.,
857 and Ma, P. L.: Earth System Model Aerosol–Cloud Diagnostics (ESMAC Diags) package, version 1:
858 assessing E3SM aerosol predictions using aircraft, ship, and surface measurements, Geosci. Model Dev.,
859 15, 4055-4076, 10.5194/gmd-15-4055-2022, 2022a.

860 Tang, S., Xie, S., Guo, Z., Hong, S.-Y., Khouider, B., Klocke, D., Köhler, M., Koo, M.-S., Krishna, P.
861 M., Larson, V. E., Park, S., Vaillancourt, P. A., Wang, Y.-C., Yang, J., Daleu, C. L., Homeyer, C. R.,
862 Jones, T. R., Malap, N., Neggers, R., Prabhakaran, T., Ramirez, E., Schumacher, C., Tao, C., Bechtold,
863 P., Ma, H.-Y., Neelin, J. D., and Zeng, X.: Long-term single-column model intercomparison of diurnal
864 cycle of precipitation over midlatitude and tropical land, Quarterly Journal of the Royal Meteorological
865 Society, 148, 641-669, 10.1002/qj.4222, 2022b.

866 Turner, D. D., Lo, C., Min, Q., Zhang, D., and Gaustad, K.: Cloud Optical Properties from the Multifilter
867 Shadowband Radiometer (MFRSRCLDOD): An ARM Value-Added Product, ARM Research
868 FacilityDOE/SC-ARM-TR-047, 2021.

869 Varble, A. C., Ma, P. L., Christensen, M. W., Mülmenstädt, J., Tang, S., and Fast, J.: Evaluation of
870 Liquid Cloud Albedo Susceptibility in E3SM Using Coupled Eastern North Atlantic Surface and Satellite
871 Retrievals, EGUsphere, 2023, 1-39, 10.5194/egusphere-2023-998, 2023.

872 Wang, J., Wood, R., Jensen, M. P., Chiu, J. C., Liu, Y., Lamer, K., Desai, N., Giangrande, S. E., Knopf,
873 D. A., Kollias, P., Laskin, A., Liu, X., Lu, C., Mechem, D., Mei, F., Starzec, M., Tomlinson, J., Wang, Y.,
874 Yum, S. S., Zheng, G., Aiken, A. C., Azevedo, E. B., Blanchard, Y., China, S., Dong, X., Gallo, F., Gao,
875 S., Ghate, V. P., Glienke, S., Goldberger, L., Hardin, J. C., Kuang, C., Luke, E. P., Matthews, A. A.,
876 Miller, M. A., Moffet, R., Pekour, M., Schmid, B., Sedlacek, A. J., Shaw, R. A., Shilling, J. E., Sullivan,
877 A., Suski, K., Veghte, D. P., Weber, R., Wyant, M., Yeom, J., Zawadowicz, M., and Zhang, Z.: Aerosol
878 and Cloud Experiments in the Eastern North Atlantic (ACE-ENA), Bull. Amer. Meteor. Soc., 1-51,
879 10.1175/bams-d-19-0220.1, 2021.

880   Watson-Parris, D., Schutgens, N., Reddington, C., Pringle, K. J., Liu, D., Allan, J. D., Coe, H., Carslaw,
881   K. S., and Stier, P.: In situ constraints on the vertical distribution of global aerosol, Atmos. Chem. Phys.,
882   19, 11765-11790, 10.5194/acp-19-11765-2019, 2019.

883   Wu, P., Dong, X., Xi, B., Tian, J., and Ward, D. M.: Profiles of MBL Cloud and Drizzle Microphysical
884   Properties Retrieved From Ground-Based Observations and Validated by Aircraft In Situ Measurements
885   Over the Azores, Journal of Geophysical Research: Atmospheres, 125, e2019JD032205,
886   10.1029/2019JD032205, 2020.

887   Xie, S., Lin, W., Rasch, P. J., Ma, P.-L., Neale, R., Larson, V. E., Qian, Y., Bogenschutz, P. A., Caldwell,
888   P., Cameron-Smith, P., Golaz, J.-C., Mahajan, S., Singh, B., Tang, Q., Wang, H., Yoon, J.-H., Zhang, K.,
889   and Zhang, Y.: Understanding Cloud and Convective Characteristics in Version 1 of the E3SM
890   Atmosphere Model, J. Adv. Model. Earth Syst., 10, 2618-2644, 10.1029/2018MS001350, 2018.

891   Xu, K.-M. and Cheng, A.: Evaluating Low-Cloud Simulation from an Upgraded Multiscale Modeling
892   Framework Model. Part II: Seasonal Variations over the Eastern Pacific, J. Climate, 26, 5741-5760,
893   10.1175/JCLI-D-12-00276.1, 2013a.

894   Xu, K.-M. and Cheng, A.: Evaluating Low-Cloud Simulation from an Upgraded Multiscale Modeling
895   Framework Model. Part I: Sensitivity to Spatial Resolution and Climatology, J. Climate, 26, 5717-5740,
896   10.1175/JCLI-D-12-00200.1, 2013b.

897   Zhang, C., Xie, S., Tao, C., Tang, S., Emmenegger, T., Neelin, J. D., Schiro, K. A., Lin, W., and Shaheen,
898   Z.: The ARM Data-Oriented Metrics and Diagnostics Package for Climate Models: A New Tool for
899   Evaluating Climate Models with Field Data, Bull. Amer. Meteor. Soc., 101, E1619-E1627,
900   10.1175/bams-d-19-0282.1, 2020.

901   Zhang, S., Zhang, K., Wan, H., and Sun, J.: Further improvement and evaluation of nudging in the E3SM
902   Atmosphere Model version 1 (EAMv1): simulations of the mean climate, weather events, and
903   anthropogenic aerosol effects, Geosci. Model Dev., 15, 6787-6816, 10.5194/gmd-15-6787-2022, 2022.

904   Zhang, Y., Xie, S., Lin, W., Klein, S. A., Zelinka, M., Ma, P.-L., Rasch, P. J., Qian, Y., Tang, Q., and Ma,
905   H.-Y.: Evaluation of Clouds in Version 1 of the E3SM Atmosphere Model With Satellite Simulators,
906   Journal of Advances in Modeling Earth Systems, 11, 1253-1268, 10.1029/2018MS001562, 2019.

907   Zhou, X., Kollias, P., and Lewis, E. R.: Clouds, Precipitation, and Marine Boundary Layer Structure
908   during the MAGIC Field Campaign, J. Climate, 28, 2420-2442, 10.1175/jcli-d-14-00320.1, 2015.

909